mathematics

MDPI

Article

Acoustic Radiation from a Lined Flanged Duct at an Order-Two Exceptional Point: Mode Matching with an Improper-Integral Radiation Closure

Mohammed Alkinidri

Department of Mathematics, College of Science & Arts, King Abdulaziz University, Rabigh 21911, Saudi Arabia; moalkinidri@kau.edu.sa

Abstract

Exceptional points are parameter values at which two eigenvalues and their corresponding eigenfunctions coalesce, rendering the wave operator defective. They arise widely in non-Hermitian wave physics and disrupt the modal expansions on which semi-analytic scattering methods rely. For lined acoustic waveguides, an augmented mode-matching ansatz that restores completeness at such a degeneracy—by adjoining the generalised eigenfunction obtained from the derivative of the parametrised duct mode with respect to its transverse spectral parameter—has been established for junctions between duct sections with discrete modal sets. This article extends that ansatz to an open, radiating configuration: a rigid feed duct communicates through an impedance-lined throat, tuned to an order-two exceptional point, with a half-space bounded by a rigid flange. The radiating mouth replaces the discrete modal closure by a continuous spectrum, so the augmented basis must be matched against an improper spectral integral. The half-space field is generated by the aperture velocity, which builds the rigid-flange condition into the representation exactly, and the resulting improper integrals are rendered analytic by branch-aware substitutions whose cutoff is tied to the retained modal content. The formulation is validated on the matching and boundary conditions themselves: pointwise continuity of pressure and of normal velocity at the internal junction, pointwise pressure continuity at the radiating mouth, the vanishing of the normal velocity on the rigid flange, and the recovery of the classical flanged-duct radiation problem in the rigid limit, cross-checked against an independent implementation. The full lined problem, including the defective case, has been further verified against an independent finite-volume solution of the same boundary-value problem, whose grid-converged fractions agree with the mode-matching values to within 8×10^{-5}. A conserved-power identity is monitored as a necessary but not sufficient check. Numerical experiments confirm the known breakdown of the standard expansion at the exceptional point and the well-conditioned convergence of the augmented one in this radiating setting, and a scan of the complex admittance plane, refined by local optimisation and repeated across throat lengths and frequencies, shows that flange radiation detunes the absorption optimum away from the exceptional point, by an amount that grows with the radiated share of the power budget and vanishes as the throat lengthens.

Keywords: exceptional point; non-self-adjoint spectrum; generalised eigenfunction; mode matching; Neumann-to-Dirichlet map; impedance boundary

MSC: 35J05; 35P25; 47A11; 47A55; 65N35; 65N12; 74J20; 76Q05

Check for updates

Received: 25 July 2026
Revised: 23 August 2026
Accepted: 27 August 2026
Published: 31 August 2026

Copyright: © 2026 by the author. Licensee MDPI, Basel, Switzerland. This article is an open access article distributed under the terms and conditions of the Creative Commons Attribution (CC BY) license.

1. Introduction

Non-Hermitian and non-self-adjoint wave operators arise whenever a system exchanges energy with its surroundings—through absorption, radiation, gain, or loss—and they exhibit a spectral feature with no self-adjoint counterpart: the exceptional point, a parameter value at which two eigenvalues and their eigenfunctions coalesce, so that the operator becomes defective and its eigenfunctions cease to form a basis. Exceptional points are by now a unifying theme across wave physics, from $\mathcal{PT}$-symmetric quantum mechanics [1], through the abstract theory of non-normal spectra [2–4], to photonics [5,6] and acoustic metamaterials [7]; the analytical structure they impose on a modal expansion is the same in every setting. They also pose a common difficulty for the semi-analytic, projection-based methods that dominate guided-wave and scattering analysis: at the degeneracy, the ordinary modal expansion loses a dimension and ceases to be complete; as the exceptional point is approached, the conventional matched system becomes increasingly ill-conditioned (the rank behaviour exactly at the degeneracy depends on how the double root is represented numerically; see Section 6). For lined acoustic waveguides, this difficulty was resolved by Lawrie et al. [8], whose augmented (enhanced) mode-matching ansatz adjoins the generalised eigenfunction of the defective transverse operator and restores completeness at the degeneracy. That ansatz is the starting point of the present article, which develops it for open, radiating configurations, in which the matched system is closed not by a discrete modal set on the far side of a junction but by the continuous spectrum of a flanged half-space, expressed as an improper spectral integral.

The propagation, reflection, transmission, and absorption of acoustic waves in finite ducts and through aperture-radiator geometries are classical subjects in linear acoustics, central both to the theoretical literature on guided waves [9–12] and to the engineering practice of silencer and turbomachinery noise control, a practice represented by recent partitioned-shell and muffler analyses such as [13]. Two algebraic frameworks dominate the analysis. The first, mode matching in the spirit of Mittra and Lee [14] together with its tailored Galerkin refinements [15,16], discretises continuity of pressure and normal velocity at every duct junction by projecting onto the local transverse modes; the algebraic system that results is finite, dense, and small. This framework has been extended, among others, to wave-bearing cavities and partitioned membrane-bounded configurations [17,18]. The second, Fourier-transform mode matching as systematised in the monograph of Eom [19], represents the open exterior region as a spectral continuum and closes the system with a Neumann-to-Dirichlet radiation operator obtained from the half-space Green's function; in the flanged-piston limit, this recovers the classical baffled-aperture radiation problem treated in [19] (the complementary unflanged-pipe problem being the classical Wiener–Hopf solution of Levine and Schwinger [20]). The present article combines the two frameworks in a single three-region acoustic geometry, in which a rigid feed duct is connected through an impedance-lined throat to a half-space behind a rigid flange. The mode-matching part operates at the duct–throat junction and projects onto the rigid feed modes; the Fourier-transform part appears at the throat–half-space mouth as an improper integral that carries the radiated power away to infinity.

What distinguishes the present configuration is the spectral character of the lined throat. A locally reacting acoustic admittance produces a Robin (Leontovich-type) boundary condition on the throat walls, and the transverse eigenproblem inside the throat becomes non-self-adjoint. The classical Cremer optimum [21–23] for the admittance value that maximises modal attenuation in a long, complex-lined duct is, mathematically, a condition under which two transverse eigenvalues of the same parity merge; for a complex admittance, this merging is not a benign eigenvalue degeneracy but an exceptional point in the sense of Kato [24], at which two eigenvalues and the corresponding eigenfunctions

both coalesce, and the spectral problem becomes defective. For the electromagnetic case of an impedance waveguide, exceptional points in the transverse spectrum were located explicitly by Midya and Konotop [25] (a recent enhanced computational mode-matching formulation for an impedance-loaded electromagnetic groove is given by Taha et al. [26]); for an acoustic lined duct, the resulting incompleteness of the projection method and its repair by an augmented modal basis were analysed by Lawrie et al. [8], who showed that the generalised eigenfunction obtained by differentiating the parametrised mode with respect to its transverse spectral parameter supplies the missing expansion direction: at the degeneracy the transverse operator has an eigenvalue of algebraic multiplicity two but geometric multiplicity one, and the ordinary eigenfunction together with this generalised eigenfunction spans the associated two-dimensional generalised eigenspace. Optimisation and conservation analyses of mode-matching schemes for finite lined ducts and chambers, on which the power-balance diagnostics used below rest, are developed in [27–30]; a closely related analysis of absorbent linings coupled to flexible duct walls appears in [31]; and optimum attenuation in a continuum of exceptional points is treated in [32].

The locally reacting admittance adopted here is the simplest surface model of an energy-exchanging wall. In many applications, the boundary is itself an elastic structure—a membrane, a plate, or a shell—and the acoustic field couples to structural wave propagation, so that the transverse spectrum acquires vibroacoustic branches: flexible-wall analogues of the present eigenproblem are analysed in [15,27,30], fluid–structure coupled scattering in flexible cylindrical shells is treated in [33,34], and recent work on the vibroacoustic transmission of lattice-cored sandwich cylindrical structures [35] illustrates how strongly the structural architecture of the wall can reshape the transmitted acoustic field. Exceptional points arise in such coupled fluid–structure spectra for the same mathematical reason as here—the coalescence of eigenvalues of a non-self-adjoint transverse operator—so the configuration studied below, in which the wall reaction is condensed into the single admittance parameter η, is also the natural first step toward augmented mode matching in fully coupled vibroacoustic radiators; this outlook is taken up again in Section 7.

The motivation for the specific problem treated here is twofold. On the physical side, the configuration—a rigid feed duct, a short lined section tuned near the Cremer condition, and an open termination radiating from a baffle—is the canonical simplified model of a lined intake or silencer outlet: precisely the setting in which Cremer-type linings are deployed in practice, and one in which the termination is open rather than anechoic or rigidly closed. Whether the attenuation benefit associated with the mode-merging lining survives the radiation loading of an open mouth, and where the absorption optimum of the finite lined section then sits relative to the exceptional point, are design questions that a closed or semi-infinite model cannot answer. On the methodological side, the geometry poses a question about the augmented ansatz itself: in the configurations treated in [8] the matched system is closed by discrete modal sets on both sides of each junction, whereas an open flanged mouth couples the augmented basis to a radiationcontinuum, so that every matrix entry involving the degenerate pair becomes an improper spectral integral with branch points at the grazing wavenumbers. The generalised waveform, including its non-separable axial term, is integrated directly against this continuum, and the resulting system remains well-conditioned and convergent at the exceptional point.

The main ingredients of the analysis are as follows. The exceptional point is located constructively from the simultaneous vanishing of the characteristic function and of its derivative with respect to the transverse spectral parameter, and the order-two property is certified by a closed-form identity for the second derivative. The defectiveness of the modal expansion is given a quantitative form through a non-conjugated norm integral that vanishes at the exceptional point. The generalised waveform is rederived for the finite throat

with anchored axial coordinates, following the construction of [8]. The half-space closure is formulated so that the rigid-flange condition is exact: the exterior field is generated by the spectrum of the aperture velocity, which vanishes on the flange, in the classical rigid-baffle (Rayleigh-type) manner [9,19], and pressure continuity across the mouth is the condition imposed by projection. The branch points of the resulting improper integrals are removed by trigonometric and hyperbolic substitutions that render every integrand analytic [36,37], and the spectral cutoff is tied to the largest retained transverse wavenumber, since the augmented basis has to be resolved against the continuum. A conserved-power identity, derived by Green's identity on the lined throat, is monitored throughout, though it isnecessary rather than sufficient: the evanescent part of the radiation spectrum carries no time-averaged power, so a power balance is blind to errors in the reactive part of the closure and cannot by itself validate a mode-matching computation. The validation therefore rests on the matching and boundary conditions themselves—pointwise continuity of pressure and normal velocity at the internal junction, pointwise pressure continuity at the radiating mouth (which the projection imposes only weakly, so that its pointwise residual measures convergence), the vanishing of the normal velocity on the rigid flange, and the even symmetry of the exterior field—together with the analytic reduction, in the limit of a vanishing lining, to the classical flanged-duct radiation problem [19], cross-checked against an independent implementation of that classical problem. The numerical experiments then set the degenerate standard expansion against the well-conditioned augmented one in the radiating setting, and a two-dimensional sweep of the absorbed-power fraction over the complex admittance plane shows that the flange radiation displaces the absorption optimum away from the exceptional point.

The article is organised as follows. Section 2 states the physical model and the governing equations, including the modal expansions of the four fields and all interface and matching conditions. Section 3 develops the transverse spectrum of the lined throat, constructs the order-two exceptional point, establishes the defectiveness of the ordinary modal expansion, and constructs the generalised waveform for the finite throat. Section 4 derives the rigid-flange radiation closure as an improper spectral integral over the aperture velocity and presents the branch-aware Gauss–Legendre quadrature used to evaluate it. Section 5 carries out the projection onto the rigid feed family, assembles the algebraic system in block form, and derives the conserved-power identity by Green's identity on the lined throat. Section 6 reports the numerical experiments: the validation of the formulation by its matching and boundary residuals, convergence and improper-integral sensitivity studies, the rigid-limit cross-check, parameter sweeps, full-geometry field maps, and a two-dimensional optimisation in the admittance plane. Section 7 concludes.

2. Physical Model and Governing Equations

Let z denote the duct axis and x the transverse coordinate of a two-dimensional acoustic waveguide of width $2a$. With the non-dimensional coordinates $X = z/a$ and $Y = x/a$, the reduced frequency $K = \omega a/c$ with ω the angular frequency and c the sound speed, and the time-harmonic convention $e^{-i\omega t}$, the acoustic pressure $p(X, Y)$ obeys the Helmholtz equation

$$\left(\partial_X^2 + \partial_Y^2 + K^2\right) p(X, Y) = 0 \tag{1}$$

in every homogeneous region together with the outgoing/decaying radiation condition at infinity. The three regions of the geometry, sketched in Figure 1, are the semi-infinite rigid feed duct $\Omega_I = \{X < 0,\ |Y| < 1\}$, the impedance-lined throat $\Omega_{II} = \{0 < X < L,\ |Y| < 1\}$ of non-dimensional length $L > 0$, and the flanged half-space $\Omega_{III} = \{X > L\}$. The walls $\{|Y| = 1,\ X < 0\}$ are rigid (the feed duct), the walls $\{|Y| = 1,\ 0 < X < L\}$ are impedance-lined (the throat), and $\{X = L,\ |Y| > 1\}$ is a rigid flange. Because the incident field is the

even fundamental mode of the feed and the geometry is symmetric about $Y = 0$, only the even-in-Y subspace is retained.

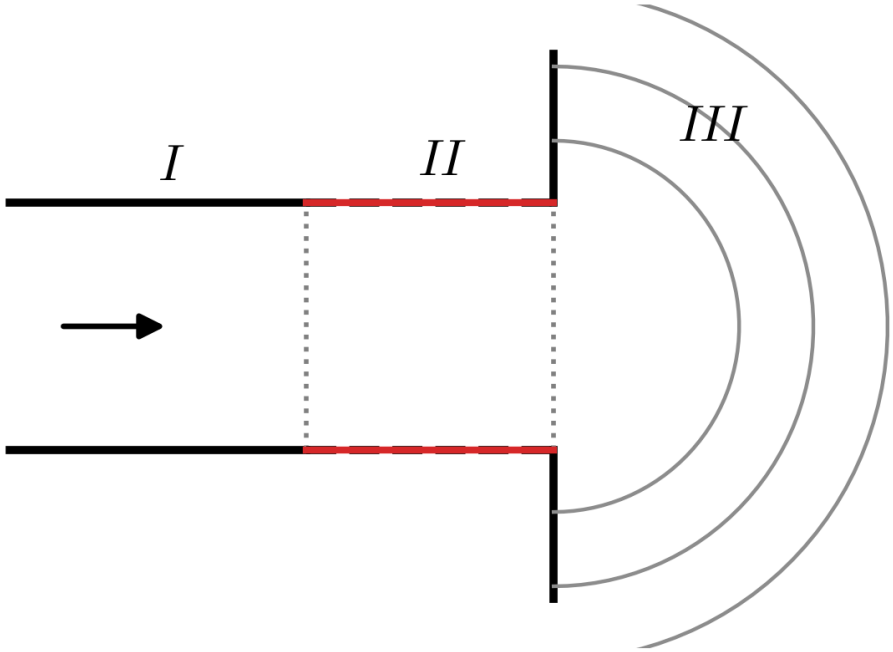


Figure 1. Three-region geometry of the model: Rigid feed duct Ω_I on the left, impedance-lined throat Ω_{II} of length L in the middle with lined walls drawn as a solid red line over a black dashed underlay, and flanged half-space Ω_{III} on the right. The dotted vertical lines mark the two matching planes $X = 0$ and $X = L$; the arrow denotes the incident fundamental and the arcs the radiated wavefronts.

The rigid walls of the feed duct and the rigid flange enforce homogeneous Neumann conditions,

$$\partial_Y p(X, \pm 1) = 0 \quad (X < 0), \qquad \partial_X p(L, Y) = 0 \quad (|Y| > 1). \tag{2}$$

The lined walls of the throat carry a locally reacting acoustic admittance with reduced complex parameter $\eta \in \mathbb{C}$, $\operatorname{Im} \eta \geq 0$ (a passive lining has $\operatorname{Im} \eta > 0$, and the lossless rigid limit is $\eta = 0$); the Leontovich/Robin condition for the pressure is

$$\partial_Y p(X, \pm 1) = \pm \eta \, p(X, \pm 1), \qquad 0 < X < L. \tag{3}$$

The rigid feed duct supports the even hard-wall family

$$U_\ell(Y) = \cos(\gamma_\ell Y), \qquad \gamma_\ell = \ell\pi, \qquad \kappa_\ell = (K^2 - \gamma_\ell^2)^{1/2}, \qquad \epsilon_\ell = \int_{-1}^{1} U_\ell^2(Y)\, dY, \tag{4}$$

with κ_ℓ on the outgoing/decaying branch $\operatorname{Im} \kappa_\ell \geq 0$, with $\epsilon_0 = 2$ and $\epsilon_\ell = 1$ for $\ell \geq 1$, and with the orthogonality $\int_{-1}^{1} U_\ell U_m \, dY = \epsilon_\ell \delta_{\ell m}$. The incident, reflected, and total feed fields are

$$p_{\text{inc}}(X, Y) = e^{iKX}, \qquad p_{\text{ref}}(X, Y) = \sum_{\ell=0}^{\infty} R_\ell \, U_\ell(Y) \, e^{-i\kappa_\ell X}, \qquad p_I = p_{\text{inc}} + p_{\text{ref}}, \tag{5}$$

with $\{R_\ell\}_{\ell \geq 0} \subset \mathbb{C}$ the unknown reflected amplitudes. Inside the lined throat, even-in-Y separable solutions of (1) that satisfy (3) take the form $\cos(QY)\, e^{i\beta(Q)X}$, where Q solves the even characteristic equation of Section 3, and the axial wavenumber and the anchored axial coordinates are

$$\beta(Q) = (K^2 - Q^2)^{1/2}, \quad \operatorname{Im}\beta \geq 0, \qquad \xi_+(X) = X, \qquad \xi_-(X) = L - X, \tag{6}$$

so that $|e^{i\beta\xi_\pm}| = e^{-\operatorname{Im}\beta\,\xi_\pm} \leq 1$ throughout Ω_{II}. Denoting by $\{Q_j\}_{j\geq 1}$ the canonical even roots, taken with $\operatorname{Re} Q \geq 0$ to avoid the identification $\cos(-QY) = \cos(QY)$, the lined-throat field, in the ordinary case of simple roots, is the bidirectional modal expansion

$$p_{II}(X,Y) = \sum_{j=1}^{\infty}\Big[C_j^+ \cos(Q_jY)\, e^{i\beta_j\xi_+(X)} + C_j^- \cos(Q_jY)\, e^{i\beta_j\xi_-(X)}\Big], \tag{7}$$

with $\beta_j = \beta(Q_j)$ and unknown amplitudes $\{C_j^\pm\}$. The half-space Ω_{III}, with its rigid flange on $\{X = L,\ |Y| > 1\}$, admits an outgoing spectral superposition that satisfies (1) and the radiation condition. Its Neumann trace on the plane $X = L$ is known on the whole line: it equals the aperture velocity $v(Y) := \partial_X p_{II}(L,Y)$ on $|Y| < 1$ by velocity continuity, and it vanishes on $|Y| > 1$ by the rigid-flange condition. The half-space field is therefore generated by the velocity spectrum, in the classical rigid-baffle (Rayleigh-type) manner [9,19]: in terms of the finite Fourier transform and the outgoing-sheet root

$$\tilde{g}(q) = \int_{-1}^{1} g(Y')\, e^{iqY'}\, dY', \qquad \gamma(q) = (K^2 - q^2)^{1/2}, \quad \operatorname{Im}\gamma \geq 0, \tag{8}$$

the scattered (transmitted) field is

$$p_{III}(X,Y) = \frac{1}{2\pi}\int_{-\infty}^{\infty} \frac{\tilde{v}(q)}{i\gamma(q)}\, e^{i\gamma(q)(X-L)}\, e^{-iqY}\, dq, \qquad \tilde{v}(q) := \widetilde{\partial_X p_{II}(L,\cdot)}(q), \tag{9}$$

whose Neumann trace $\partial_X p_{III}(L,Y) = (2\pi)^{-1}\int \tilde{v}(q)e^{-iqY}dq$ reproduces, by Fourier inversion, the zero-extended aperture velocity: axial-velocity continuity across the mouth and the rigid-flange condition are both satisfied exactly by the representation. The four matching conditions at the two interfaces are pressure and axial-velocity continuity at $X = 0$,

$$p_I(0,Y) = p_{II}(0,Y), \qquad \partial_X p_I(0,Y) = \partial_X p_{II}(0,Y), \qquad |Y| < 1, \tag{10}$$

and pressure and axial-velocity continuity at $X = L$,

$$p_{II}(L,Y) = p_{III}(L,Y), \qquad \partial_X p_{II}(L,Y) = \partial_X p_{III}(L,Y), \qquad |Y| < 1. \tag{11}$$

The active radiation matching is therefore the first condition of (11), pressure continuity at the radiating mouth, which with (9) takes the Neumann-to-Dirichlet form

$$p_{II}(L,Y) = \mathcal{N}[\partial_X p_{II}(L,\cdot)](Y), \qquad \mathcal{N}[v](Y) := \frac{1}{2\pi}\int_{-\infty}^{\infty} \frac{\tilde{v}(q)}{i\gamma(q)}\, e^{-iqY}\, dq, \tag{12}$$

imposed by projection in Section 5. The projection enforces (12) only in the weak sense, so the pointwise residual of pressure continuity across the mouth is an independent measure of convergence; it is reported in Section 6. For generic η, the roots of the characteristic equation are simple and (7) is a valid representation; the case in which two simple roots coalesce, and the resulting modification of the expansion, is taken up below.

3. Lined-Throat Spectrum and the Augmented Expansion at an Exceptional Point

The transverse operator of the lined throat is the unbounded operator $T_\eta u = -u''$ on $L^2(-1,1)$ with domain $\{u \in H^2(-1,1) : u'(\pm 1) = \pm\eta u(\pm 1)\}$, which is closed, has compact resolvent, and is complex symmetric with respect to the non-conjugated pair-

ing $(f,g) = \int_{-1}^{1} fg\,dY$. Its even-in-$Y$ eigenvalues are Q^2, with eigenfunctions $\cos(QY)$, and existence reduces to the characteristic equation

$$\begin{aligned} F_e(Q,\eta) = Q\tan Q + \eta = 0, \qquad \partial_Q F_e = \tan Q + Q\sec^2 Q, \\ \partial_Q^2 F_e = 2\sec^2 Q\,(1 + Q\tan Q), \end{aligned} \tag{13}$$

with the axial wavenumber $\beta(Q)$ of (6) and $\beta_Q = \partial_Q \beta = -Q/\beta$. The function F_e is meromorphic in Q with poles at $Q = (n + \frac{1}{2})\pi$ and is even in Q, so Q and $-Q$ describe the same transverse function and are identified throughout. An order-two exceptional point of the even family is a pair $(\widetilde{Q}, \widetilde{\eta}) \in \mathbb{C}^2$ at which two simple roots of F_e merge into a double root, equivalently

$$F_e(\widetilde{Q}, \widetilde{\eta}) = 0, \qquad \partial_Q F_e(\widetilde{Q}, \widetilde{\eta}) = 0, \qquad \partial_Q^2 F_e(\widetilde{Q}, \widetilde{\eta}) \neq 0. \tag{14}$$

The two equations $\tan Q + Q\sec^2 Q = 0$ and $\eta = -Q\tan Q$ do not possess a unique solution: they define a countable family of exceptional points, one associated with each branch of $\tan Q$, together with the mirror images generated by the symmetry $Q \to -Q$. Throughout this article, the exceptional point refers to the specific member of this family considered here, namely the fundamental (lowest) canonical root in the fourth quadrant of the Q-plane, $\widetilde{Q} = 2.1061961152 - 1.1253643058\,i$, to which Newton's method on the analytic function $H(Q) = \tan Q + Q\sec^2 Q$ converges quadratically from the seed $2.1 - 1.1\,i$; the higher members of the family are accessible by the same constructive procedure from seeds on the higher branches of $\tan Q$, and optimum attenuation along a parametrised continuum of exceptional points is explored, in the closely related setting of a rigid guide fitted with wire-mesh perforates, in [32]; a complementary route to selective modal attenuation, filtering by resistive layers, is analysed in [38]. The order-two non-degeneracy of the resulting pair $(\widetilde{Q}, \widetilde{\eta})$ admits a closed-form evaluation: at the double root, $\tan\widetilde{Q} = -\widetilde{Q}\sec^2\widetilde{Q}$ and $\widetilde{\eta} = \widetilde{Q}^2\sec^2\widetilde{Q}$ together with the Pythagorean identity $\sec^2\widetilde{Q} = 1 + \widetilde{Q}^2\sec^4\widetilde{Q}$ imply $\sec^2\widetilde{Q}\,(1 - \widetilde{Q}^2\sec^2\widetilde{Q}) = 1$, hence $\partial_Q^2 F_e(\widetilde{Q}, \widetilde{\eta}) = 2$. The defective mode is then self-orthogonal with respect to the non-conjugated pairing: the explicit identity $\int_{-1}^{1}\cos^2(\widetilde{Q}Y)\,dY = 1 + \sin(2\widetilde{Q})/(2\widetilde{Q})$ reduces, using $\widetilde{Q}\tan\widetilde{Q} = -\widetilde{\eta}$ together with $\tan\widetilde{Q} + \widetilde{Q}\sec^2\widetilde{Q} = 0$, to a non-zero constant times $\partial_Q F_e(\widetilde{Q}, \widetilde{\eta})$, which vanishes by construction.

The vanishing of the non-conjugated norm of the defective mode,

$$N = \int_{-1}^{1}\cos^2(\widetilde{Q}Y)\,dY = 1 + \frac{\sin(2\widetilde{Q})}{2\widetilde{Q}} = 0 \quad \text{at } (\widetilde{Q}, \widetilde{\eta}), \tag{15}$$

has direct algebraic consequences. In the classical form of mode matching, in which the continuity conditions are projected onto the lined-throat modes themselves, the modal amplitudes carry the inverse norms explicitly, through projection coefficients of the form $B_j/(2s_jP_j)$ with $P_j = N_j$ the non-conjugated norm of the j-th transverse mode [8]; at the exceptional point, the denominator associated with the defective mode vanishes and the ordinary modal set fails to be a basis. In the assembly adopted in Section 5, every continuity condition is instead projected onto the rigid feed family, whose norms $\epsilon_\ell \in \{1, 2\}$ never vanish, so the inverse norms $1/P_j$ do not appear explicitly in the resulting linear system (26)–(29); the self-orthogonality (15) enters through the columns instead, the two coalescing columns becoming linearly dependent at the rate set by the square-root splitting (21), as quantified in Section 6. The cure is to enlarge the modal set by the generalised waveform obtained from the analytic family $\cos(QY)\,e^{i\beta(Q)\xi}$, which solves (1) on the analytic curve $Q^2 + \beta^2 = K^2$; the impedance operator does not depend on Q, while

the impedance condition holds only on the root set $F_e(Q,\eta) = 0$, and its preservation under differentiation at the double root is verified in (17) and (18) below. Differentiating with respect to Q at $Q = \widetilde{Q}$ produces, as in [8] and by smooth dependence on the spectral parameter and the interchange of derivatives, a further solution of the Helmholtz equation that satisfies the same impedance condition,

$$\Psi^{\pm}(X,Y) = \partial_Q \left[\cos(QY)\, e^{i\beta(Q)\xi_{\pm}}\right]_{Q=\widetilde{Q}} = \left[\phi_Q(Y) + i\beta_Q\, \xi_{\pm}\, \widetilde{\phi}(Y)\right] e^{i\widetilde{\beta}\,\xi_{\pm}}, \tag{16}$$

with $\widetilde{\phi}(Y) = \cos(\widetilde{Q}Y)$, $\phi_Q(Y) = -Y\sin(\widetilde{Q}Y)$, $\widetilde{\beta} = \beta(\widetilde{Q})$, and $\beta_Q = -\widetilde{Q}/\widetilde{\beta}$.

That $\Psi^{\pm}$ satisfies the Robin condition (3) is a consequence of both exceptional-point conditions in (14), and the elementary proof is worth recording. For the even family, it suffices to check the wall $Y = 1$. Introducing the boundary functional $\mathcal{B}_\eta[u] = u'(1) - \eta\, u(1)$, a direct evaluation gives, for every Q,

$$\mathcal{B}_\eta[\cos(Q\,\cdot)] = -Q\sin Q - \eta\cos Q = -\cos Q\,\left(Q\tan Q + \eta\right) = -\cos Q\; F_e(Q,\eta). \tag{17}$$

The boundary functional acts on the transverse variable only, so applied to (16) it distributes over the two transverse profiles, $\mathcal{B}_{\widetilde{\eta}}[\Psi^{\pm}(X,\cdot)] = \left[\mathcal{B}_{\widetilde{\eta}}[\phi_Q] + i\beta_Q\,\xi_{\pm}\mathcal{B}_{\widetilde{\eta}}[\widetilde{\phi}]\right] e^{i\widetilde{\beta}\xi_{\pm}}$, and (17) together with its Q-derivative at $Q = \widetilde{Q}$ gives

$$\mathcal{B}_{\widetilde{\eta}}[\widetilde{\phi}] = -\cos\widetilde{Q}\, F_e(\widetilde{Q},\widetilde{\eta}), \qquad \mathcal{B}_{\widetilde{\eta}}[\phi_Q] = \sin\widetilde{Q}\, F_e(\widetilde{Q},\widetilde{\eta}) - \cos\widetilde{Q}\,\partial_Q F_e(\widetilde{Q},\widetilde{\eta}). \tag{18}$$

Because the non-separable term of (16) carries the X-dependent factor $i\beta_Q\xi_{\pm}$, the two brackets must vanish separately for the impedance condition to hold identically in X. The first vanishes by the first condition of (14) alone, but the second vanishes only because F_e and $\partial_Q F_e$ vanish simultaneously (note that $\cos\widetilde{Q} \neq 0$, the poles of tan being excluded from the root set). The generalised waveform therefore satisfies the Robin condition (3) precisely at an order-two exceptional point, and at no other parameter value.

The function $\Psi^{\pm}$ is not separable in (X,Y); the non-separable axial-growth term $i\beta_Q\xi_{\pm}\widetilde{\phi}$ is precisely the piece that supplies the missing expansion direction. In operator terms, at $\eta = \widetilde{\eta}$, the eigenvalue $\widetilde{Q}^2$ of the transverse operator T_η has algebraic multiplicity two and geometric multiplicity one, and the transverse profiles $\widetilde{\phi}$ and ϕ_Q span its two-dimensional generalised eigenspace (a Jordan chain of length two), in the standard analytic sense of coalescing eigenvectors at an order-two algebraic branch point of an analytic operator family [2,24]; the mode-matching equations themselves remain an infinite algebraic system, built from this transverse basis. The augmented modal expansion of the lined-throat field at the exceptional point is therefore

$$\begin{aligned} p_{II}(X,Y) = &\sum_{Q_j \neq \widetilde{Q}} \left[C_j^{+}\cos(Q_jY)e^{i\beta_j\xi_{+}} + C_j^{-}\cos(Q_jY)e^{i\beta_j\xi_{-}}\right] \\ &+ \sum_{s=\pm}\left[\widetilde{C}^{s}\widetilde{\phi}(Y)e^{i\widetilde{\beta}\xi_s} + \overline{C}^{s}\Psi^{s}(X,Y)\right], \end{aligned} \tag{19}$$

in which the two coalescing simple modes have been replaced, in each axial direction, by the pair $(\widetilde{\phi}\, e^{i\widetilde{\beta}\xi_{\pm}}, \Psi^{\pm})$, so that the column count is unchanged and the algebraic system remains square. Away from the exceptional point, the two roots are distinct and (7) is used. The canonical even-root set is certified by the argument-principle count applied to the entire function $G(Q) = Q\sin Q + \eta\cos Q = \cos Q \cdot F_e(Q,\eta)$, which has the same zeros as F_e and no poles; the number of zeros inside any rectangle $\Omega \subset \mathbb{C}$ avoiding the zeros of G is

$$\mathcal{Z}(\Omega) = \frac{1}{2\pi i}\oint_{\partial\Omega}\frac{G'(Q)}{G(Q)}\,dQ, \qquad G'(Q) = (1-\eta)\sin Q + Q\cos Q, \tag{20}$$

a robust diagnostic against the pitfall of parameter continuation through the coalescence. Near the double root, the two coalescing branches separate, by the local quadratic expansion of F_e at (14), according to the square-root law

$$Q_{\pm}(\eta) \;\approx\; \widetilde{Q} \pm \left(-\frac{2(\eta-\widetilde{\eta})}{\partial_Q^2 F_e(\widetilde{Q},\widetilde{\eta})} \right)^{1/2}, \tag{21}$$

which is used both to seed the complex Newton iteration through the coalescence and, in Section 6, to explain the observed conditioning of the standard scheme.

4. Rigid-Flange Radiation Closure and Its Numerical Evaluation

The representation (9) is the plane-wave form of the classical rigid-baffle construction: the Neumann Green's function of the half-space, $G_+ = G_{\text{free}} + G^*_{\text{free}}$ with G^*_{free} the mirror image across $X = L$ [9,10], reduces the exterior field, by Green's second identity and the radiation condition, to an integral of the aperture velocity against G_+; substituting the plane-wave decomposition $G_+(X,Y;L,Y') = (2\pi)^{-1} \int e^{i\gamma(q)(X-L)}/(i\gamma(q))\, e^{-iq(Y-Y')} dq$ recovers (9). The operative object in the matched system is the Neumann-to-Dirichlet trace $\mathcal{N}$ of (12), an improper integral whose integrand carries the factor $1/(i\gamma)$ with inverse-square-root branch points at the grazing wavenumbers $q = \pm K$. Branch-aware substitutions remove them exactly. On the propagating spectral band $|q| < K$, set $q = K\sin\theta$ with $\theta \in (-\pi/2, \pi/2)$; then $\gamma = K\cos\theta$ and $dq = K\cos\theta\, d\theta$, so the singular factor cancels identically, $dq/(i\gamma) = d\theta/i$, and the contribution becomes

$$\mathcal{N}_{\text{prop}}[v](Y) = \frac{1}{2\pi i} \int_{-\pi/2}^{\pi/2} \tilde{v}(K\sin\theta)\, e^{-iK\sin\theta\, Y}\, d\theta, \tag{22}$$

an integrand analytic in θ on a complex neighbourhood of $[-\pi/2, \pi/2]$ whenever $\tilde{v}$ extends analytically into a complex disc containing $\{K\sin\theta : \theta \in E_\rho\}$, where E_ρ is the Bernstein ellipse with foci ± 1 and sum of semi-axes $\rho > 1$; the classical Gauss–Legendre bound [36,37,39] then gives geometric convergence in the node count. On the evanescent range, orienting both pieces so that they add up to the line integral over $q \in (-\infty, \infty)$, the substitution $q = \pm K\cosh t$ with $t > 0$ gives $\gamma = iK\sinh t$ and, on either side, the oriented element $dq/(i\gamma) = -dt$, so that

$$\mathcal{N}^{\pm}_{\text{ev}}[v](Y) = -\frac{1}{2\pi} \int_0^{T_1} \tilde{v}(\pm K\cosh t)\, e^{\mp iK\cosh t\, Y}\, dt, \tag{23}$$

a kernel real up to the transform factors and therefore carrying no time-averaged radiated power. The orientation fixed above is the one for which the two evanescent contributions add rather than cancel in the even projections, so that the reactive part of the closure is retained in full. The cosh map clusters nodes at the branch point but spaces them geometrically farther out, so it is used only up to $q = 3K$ ($T_1 = \operatorname{arcosh} 3$); beyond, a plain Gauss–Legendre rule in q on $[3K, q_{\max}]$, with $\gamma = i(q^2 - K^2)^{1/2}$ smooth there, covers the far tail, on which the transforms oscillate with bounded frequency ($|e^{iqY'}|$ with $|Y'| \le 1$), so a fixed number of nodes per unit q suffices. The choice of the cutoff $q_{\max}$ is dictated by the modal content, not by the frequency: the transform of a transverse function with root Q_n peaks near $q \approx |\operatorname{Re} Q_n|$, so $q_{\max}$ must clear the largest retained transverse wavenumber ($\approx M\pi$ for M retained even functions) by a safe margin, since the rows of the radiation closure associated with the highest modes are otherwise truncated. The practical algorithm concatenates the three rules—n_{prop} nodes on $[-\pi/2, \pi/2]$, n_{tail} nodes on $[0, T_1]$ per side, and a far-tail rule scaled to $q_{\max} \gtrsim 1.35\, M\pi$—evaluates the velocity transforms $\tilde{v}(q_n)$ and the feed-mode transforms $\widetilde{U}_\ell(-q_n)$ of (8) by Gauss–Legendre over $Y \in [-1, 1]$, and forms every radiation matrix entry as a single weighted sum.

5. Mode-Matching Projection and the Conserved-Power Identity

The unknowns of the algebraic system are the truncated reflected feed amplitudes $\{R_\ell\}_{\ell=0}^{M-1}$ and the truncated lined-throat amplitudes $\{C_k\}_{k=1}^{2M}$, in which k enumerates the kept transverse functions in each axial direction: ordinary $\cos(Q_j Y)\, e^{i\beta_j \xi_\pm}$ away from the exceptional point, and $\widetilde{\phi}\, e^{i\widetilde{\beta}\xi_\pm}$ together with $\Psi^\pm$ at the exceptional point. Following the classical mode-matching projection framework [14–16,30], every continuity condition is projected onto the rigid feed family $\{U_\ell\}_{\ell=0}^{M-1}$ on $|Y| < 1$ via the non-conjugated complex pairing on $L^2(-1,1)$, and every transverse integral over $[-1,1]$ is evaluated by Gauss–Legendre quadrature; the half-space Neumann-to-Dirichlet entries are evaluated by the algorithm of the previous section. The four families of coupling integrals are

$$L_{\ell k}^{(0)} = \langle U_\ell, \Phi_k(0,\cdot)\rangle, \quad D_{\ell k}^{(0)} = \langle U_\ell, \partial_X \Phi_k(0,\cdot)\rangle, \quad L_{\ell k}^{(L)} = \langle U_\ell, \Phi_k(L,\cdot)\rangle, \tag{24}$$

$$N_{\ell k}^{\mathrm{rad}} = \langle U_\ell, \mathcal{N}[\partial_X \Phi_k(L,\cdot)]\rangle = \frac{1}{2\pi}\sum_{n=1}^{N} \frac{dq_n}{i\gamma(q_n)}\, \widetilde{\partial_X \Phi}_k(L,q_n)\, \widetilde{U}_\ell(-q_n), \tag{25}$$

where Φ_k denotes the k-th lined-throat waveform, $\langle\cdot,\cdot\rangle$ is the non-conjugated pairing, and the spectral sum in (25) runs over the concatenated propagating/evanescent/far-tail Gauss–Legendre node array of Section 4, with the oriented weights given there. Using the orthogonality of the feed family (4) and the contribution of the incident field on the right-hand side, $\langle U_\ell, 1\rangle = \epsilon_\ell \delta_{\ell 0}$ for pressure and $\langle U_\ell, \partial_X p_{\mathrm{inc}}\rangle = iK\epsilon_\ell \delta_{\ell 0}$ for axial velocity, the projected pressure and axial-velocity matchings at $X = 0$ and the projected mouth pressure-continuity (Neumann-to-Dirichlet) matching at $X = L$ read, for $\ell = 0, \ldots, M-1$,

$$\epsilon_\ell(\delta_{\ell 0} + R_\ell) = \sum_{k=1}^{2M} C_k\, L_{\ell k}^{(0)}, \tag{26}$$

$$\epsilon_\ell(iK\delta_{\ell 0} - i\kappa_\ell R_\ell) = \sum_{k=1}^{2M} C_k\, D_{\ell k}^{(0)}, \tag{27}$$

$$\sum_{k=1}^{2M} C_k\, L_{\ell k}^{(L)} = \sum_{k=1}^{2M} C_k\, N_{\ell k}^{\mathrm{rad}}. \tag{28}$$

Assembling the unknown vector $x = [R_0, \ldots, R_{M-1}, C_1, \ldots, C_{2M}]^\top$, the diagonal matrices $E = \mathrm{diag}(\epsilon_\ell)$ and $\boldsymbol{\kappa} = \mathrm{diag}(\kappa_\ell)$, and the rectangular blocks $L^{(0)}, D^{(0)}, L^{(L)}$, $N^{\mathrm{rad}} \in \mathbb{C}^{M\times 2M}$, the system (26)–(28) is the square linear problem

$$\begin{bmatrix} E & -L^{(0)} \\ -i\boldsymbol{\kappa}E & -D^{(0)} \\ 0 & L^{(L)} - N^{\mathrm{rad}} \end{bmatrix} x = \begin{bmatrix} -\epsilon_0 \mathbf{e}_0 \\ -iK\epsilon_0 \mathbf{e}_0 \\ 0 \end{bmatrix} \quad \in \mathbb{C}^{3M\times 3M}, \tag{29}$$

with $\mathbf{e}_0 \in \mathbb{R}^M$ the first canonical vector. The system is solved by direct factorisation; at the exceptional point, the lined-column block is built from the augmented columns of (19), with the corresponding axial derivatives computed by differentiating (16); while away from the exceptional point, the lined columns are ordinary simple modes and the system reduces to the standard mode-matching form. Note that no inverse modal norms appear in (26)–(29): every projection is taken against the feed family, whose norms ϵ_ℓ never vanish, so every coefficient of the system is finite at the exceptional point. The degeneracy (15) manifests itself instead through the columns, the two coalescing lined columns differing by $O(|\eta - \widetilde{\eta}|^{1/2})$ by (21); the quantitative consequences for the conditioning are examined in Section 6.

The conserved-power identity follows from the same matching conditions through Green's identity applied to p and its complex conjugate on the lined throat [9,12,27,28].

From $0 = \int_{\Omega_{II}} \mathrm{Im}\{\overline{p}\,(\Delta p + K^2 p)\}\,dV = \int_{\partial\Omega_{II}} \mathrm{Im}\{\overline{p}\,\partial_n p\}\,ds$ and the impedance condition $\partial_n p = \eta p$ on the lined walls, the wall contribution evaluates to $\mathrm{Im}\,\eta \int_0^L (|p_{II}(X,1)|^2 + |p_{II}(X,-1)|^2)\,dX$, and the matching-plane contributions evaluate, via modal orthogonality and the spectral representation (9), to the reflected guided flux at $X = 0$ and the radiated half-space flux at $X = L$. Combining and normalising by the incident flux $P_{\mathrm{inc}} = 2K$ gives the identity

$$1 = R + S + A, \qquad \mathrm{TL} = -10\log_{10} S, \tag{30}$$

in which the reflected, scattered, and absorbed fractions are

$$\begin{aligned} R &= \frac{1}{2K}\sum_{\kappa_\ell \in \mathbb{R}_+} \kappa_\ell\,\epsilon_\ell\,|R_\ell|^2, \qquad S = \frac{1}{4\pi K}\int_{-K}^{K} \frac{|\tilde{v}(q)|^2}{\gamma(q)}\,dq = \frac{1}{4\pi K}\int_{-\pi/2}^{\pi/2} \left|\tilde{v}(K\sin\theta)\right|^2 d\theta, \\ A &= \frac{\mathrm{Im}\,\eta}{2K}\int_0^L \left(|p_{II}(X,1)|^2 + |p_{II}(X,-1)|^2\right) dX, \end{aligned} \tag{31}$$

with $\tilde{v}$ the aperture-velocity transform of (9); the substitution $q = K\sin\theta$ again cancels the endpoint singularity of $1/\gamma$ exactly. Only the propagating band $|q| < K$ contributes to S: the evanescent spectrum carries no time-averaged power. The identity (30) is consequently necessary—any solution of the correctly closed system must satisfy it—but not sufficient, since an error confined to the reactive (evanescent) part of the radiation closure leaves every one of its terms unchanged. It is monitored throughout alongside the pointwise matching and boundary residuals of Section 6.

The propagating spectrum also yields the far field in closed form, which provides one further independent consistency check and the directivity of the radiator. Writing $(X - L, Y) = r(\cos\theta, \sin\theta)$ with $\theta \in (-\pi/2, \pi/2)$ and applying the stationary-phase method to (9)—the phase $\gamma(q)\cos\theta - q\sin\theta$ is stationary at $q^* = -K\sin\theta$, where $\gamma(q^*) = K\cos\theta$ and the second derivative of the phase equals $-1/(K\cos^2\theta)$—gives, using $\tilde{v}(-q) = \tilde{v}(q)$ for the even family,

$$p_{III}(r,\theta) \;\sim\; \frac{e^{i(Kr - \pi/4)}}{i\sqrt{2\pi K r}}\,\tilde{v}(K\sin\theta), \qquad Kr \to \infty, \tag{32}$$

so that the angular density of radiated power (the directivity) is

$$D(\theta) = \frac{\left|\tilde{v}(K\sin\theta)\right|^2}{4\pi K}, \qquad S = \int_{-\pi/2}^{\pi/2} D(\theta)\,d\theta, \tag{33}$$

in exact agreement with the second form of S in (31). The implementation verifies (32) against direct quadrature of (9) on a far semicircle and the directivity integral of (33) against the flux value of S; the measured agreements are reported with the validation summary in Section 6.

6. Numerical Results and Validation

Throughout this section, the reference configuration is the reduced frequency $K = 3$, the throat length $L = 2$, and the retained modal order $M = 30$ (that is, $2M$ lined columns and $3M$ equations), unless explicitly stated otherwise; the spectral quadrature uses $n_{\mathrm{prop}} = n_{\mathrm{tail}} = 400$ nodes, a far-tail rule scaled as in Section 4, and a cutoff $q_{\max} \approx 1.35\,M\pi + 8$ adapted to the retained modal content. The parameter sweeps of the frequency, admittance, and optimisation figures use 180 nodes per piece with the same adaptive cutoff, and the sensitivity to each of these quadrature parameters is reported below. A complete specification of the algorithmic parameters and tolerances used at every stage of the computation—root finding, argument-principle certification, spec-

tral quadrature, residual definitions, and the two independent implementations used for cross-checking—is collected in Section 6.5 at the end of the section, so that every number reported here can be reproduced. The exceptional point is built constructively from (14), and the residuals $|F_e|$, $|\partial_Q F_e|$, $|N|$, and $|\partial_Q^2 F_e - 2|$ are checked to be at machine zero; the canonical even-root set is certified by the argument-principle count (20); the $\eta \to 0$ limit is checked against the classical flanged-duct radiation problem, and additionally cross-checked against an independent implementation of that problem; pointwise pressure and axial-velocity continuity (10) are verified at $X = 0$; pointwise pressure continuity (11) is verified at the radiating mouth $X = L$ (a condition the projection imposes only weakly); the normal velocity on the rigid flange is verified to vanish, per the second condition of (2); the even symmetry of the exterior trace is verified to machine precision; and the conserved-power identity (30) is monitored as the secondary check. The numerical values reached at the exceptional lining $\eta = \widetilde{\eta}$ are collected in Table 1; in particular, the exceptional point is $\widetilde{Q} = 2.1061961152 - 1.1253643058\,i$ and $\widetilde{\eta} = 1.6506112935 + 2.0599814572\,i$, the mouth pressure-continuity residual of the enhanced scheme is 1.2×10^{-3}, the flange-velocity residual (measured on $1.1 \le Y \le 3$, outside the integrable rim singularity of the mouth corner) is 1.1×10^{-2}, and the transmission loss is 6.714 dB. The $\eta \to 0$ reduction to the classical flanged-duct radiation problem is satisfied to $|1 - R - S| = 2.3 \times 10^{-14}$ independently of the throat length, with no power absorbed in the rigid limit; the same rigid limit, computed by the present code and by an independent implementation of the classical flanged-guide problem (a separate derivation, quadrature, and linear system), gives fundamental reflection magnitudes of 0.04067 and 0.04068, respectively, in agreement to 8.4×10^{-6}, with reflected power fractions in agreement to 6.8×10^{-7}.

Table 1. Validation summary for the reference case at the exceptional lining $\eta = \widetilde{\eta}$, $K = 3$, $L = 2$, $M = 30$, with the adaptive spectral quadrature of Section 4. The standard expansion omits the generalised waveform (16); the enhanced expansion includes it. The $X = 0$ interface error is the larger of the pointwise pressure and velocity residuals there; the mouth error is the pointwise pressure-continuity residual at $X = L$ on $|Y| \le 0.9$; the flange residual is the normal velocity on $1.1 \le Y \le 3$ relative to the aperture-velocity rms. At exactly $\eta = \widetilde{\eta}$ the standard root set contains the double root once, so the standard matrix is invertible with the moderate condition number listed; its defect appears as the $O(10^2)$ interface error, not as a rank deficiency (see the discussion of the conditioning study below).

Quantity	**Value**
$\widetilde{Q}$	$2.1061961152 - 1.1253643058\,i$
$\widetilde{\eta}$	$1.6506112935 + 2.0599814572\,i$
condition number, standard	3.3×10^3
condition number, enhanced	152
$X = 0$ interface error, standard	641
$X = 0$ interface error, enhanced	2.8×10^{-3}
mouth pressure error, standard	1.98
mouth pressure error, enhanced	1.2×10^{-3}
flange-velocity residual, enhanced	1.1×10^{-2}
exterior symmetry residual, enhanced	1.2×10^{-16}
R	1.18×10^{-3}
S	0.213084
A	0.785743
$R + S + A$	1.000005039
$\lvert 1 - R - S - A \rvert$ (secondary check)	5.0×10^{-6}
transmission loss (dB)	6.714

6.1. Validation, Convergence, and Parameter Sweeps

The first task is to locate the exceptional point in the spectrum and to display the defective nature of the eigenfunction there. Figure 2 plots the first sixteen canonical even roots of the characteristic equation $F_e(Q, \widetilde{\eta}) = 0$ in the complex Q-plane, obtained by complex Newton iteration seeded by (21) near the coalescence. The roots populate the right half-plane, and the exceptional point $\widetilde{Q}$ sits in the fourth quadrant, distinct from the remaining simple roots. To visualise the self-orthogonality phenomenon, Figure 3 sweeps the imaginary part of the admittance across the exceptional point at fixed $\mathrm{Re}\,\eta = \mathrm{Re}\,\widetilde{\eta}$, over the window $\mathrm{Im}\,\eta \in [\mathrm{Im}\,\widetilde{\eta} - 0.22, \mathrm{Im}\,\widetilde{\eta} + 0.22]$ with sixty-one sample points, and follows the two coalescing even branches by seeding the Newton iteration with the square-root split (21); the non-conjugated norm (15) collapses to machine zero along both branches at $\mathrm{Im}\,\eta = \mathrm{Im}\,\widetilde{\eta}$.

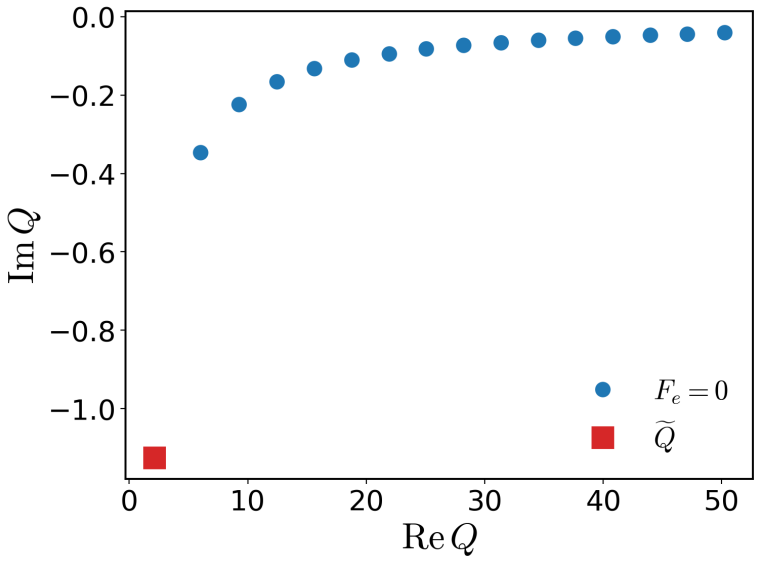


Figure 2. Even transverse wavenumbers in the complex Q-plane at $\eta = \widetilde{\eta}$. The blue circles are the sixteen leading simple roots of (13) found by complex Newton iteration; the red square is the exceptional point $\widetilde{Q}$.

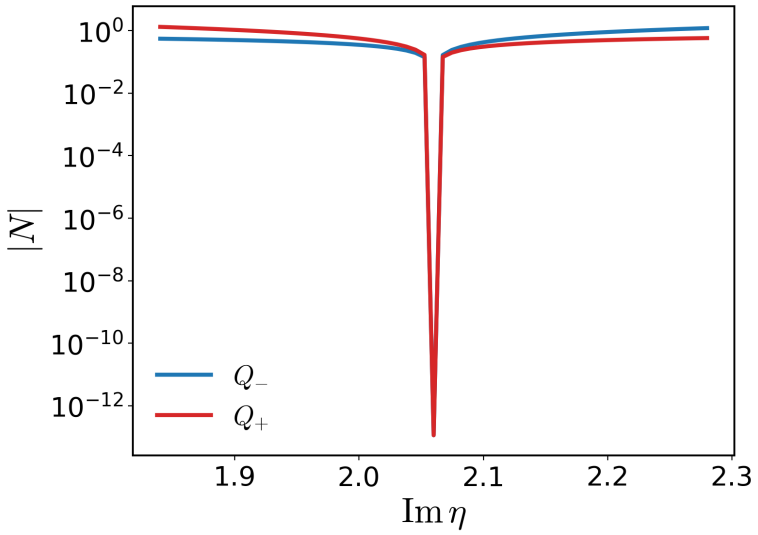


Figure 3. Self-orthogonality indicator $|N|$ along the two coalescing even branches at fixed $\mathrm{Re}\,\eta = \mathrm{Re}\,\widetilde{\eta}$, as $\mathrm{Im}\,\eta$ sweeps the window $[\mathrm{Im}\,\widetilde{\eta} - 0.22, \mathrm{Im}\,\widetilde{\eta} + 0.22]$ on sixty-one equispaced samples. Both branches collapse to machine zero at the exceptional point.

The algebraic consequences of the coalescence are shown in Figures 4 and 5. In Figure 4, the admittance is perturbed away from the exceptional point along the imaginary direction, $\eta = \widetilde{\eta} + i\,d$ with $d \in [10^{-7}, 10^{-1}]$ on twenty logarithmically spaced points, and the two-norm condition number of the matrix (29) is evaluated at $K = 3$, $L = 2$, and $M = 12$ for the standard scheme; the horizontal reference is the condition number of the enhanced scheme at $\eta = \widetilde{\eta}$. The standard scheme becomes severely ill-conditioned as the lining approaches the coalescence, with κ_2 reaching $\sim 10^5$, whereas the enhanced scheme stays bounded near $\kappa_2 \approx 152$. The growth follows the inverse-square-root law $\kappa_2 \sim |\eta - \widetilde{\eta}|^{-1/2}$—one decade of condition number per two decades of detuning in Figure 4—which is exactly what the square-root splitting (21) of the coalescing pair predicts: the two nearly coincident columns of the standard system differ by $O(|\eta - \widetilde{\eta}|^{1/2})$, so their Gram block degenerates at that rate. Two features of this curve deserve comment, because the condition number of the standard scheme at exactly $\eta = \widetilde{\eta}$ in Table 1 is finite. First, the inverse-square-root growth holds while the two members of the coalescing pair are resolved as distinct roots; once $|\eta - \widetilde{\eta}| \lesssim 10^{-6}$, their separation $|Q_+ - Q_-| \approx 2|\eta - \widetilde{\eta}|^{1/2}$ falls below the scale at which the seeded Newton iteration reliably separates the two members, the root list then retains a single member of the pair, and the condition number behaves erratically—the non-monotone points at the smallest detunings in Figure 4. Second, at exactly $\eta = \widetilde{\eta}$, the canonical root set contains the double root exactly once, the slot freed by the merger being occupied by the next simple root, so the standard matrix is invertible, with a moderate condition number ($\kappa_2 = 4.9 \times 10^2$ at $M = 12$; 3.3×10^3 at $M = 30$, the value listed in Table 1). The failure of the standard scheme at the exceptional point is therefore one of completeness, not of rank: its columns span a space that omits the generalised direction ϕ_Q entirely, which is why its interface residuals in Table 1 and Figure 5 are of order 10^2 and grow as the defective basis is refined, while its condition number remains unremarkable. The two diagnostics are complementary: the conditioning detects the approach to the degeneracy, and the matching residuals detect the degeneracy itself. Figure 5 then sweeps the modal order $M \in \{6, 8, 10, 14, 18, 22, 26, 30, 36, 42\}$ at $\eta = \widetilde{\eta}$, $K = 3$, $L = 2$, and shows the pointwise interface error at $X = 0$ for both schemes: the standard error is large—of order 10^2, and in fact growing as the defective basis is refined—while the enhanced error decreases monotonically with M, as it does in the closed configurations of [8].

Table 2 makes the effect of the truncation parameters on the physically observable quantities explicit: the reflected, radiated, and absorbed fractions at the exceptional lining are listed against the modal order M (the spectral cutoff being adapted to M as in Section 4), together with the power-identity error and the condition number of the enhanced system. The radiated and absorbed fractions are converged to three significant figures by $M = 10$ and to four by $M \approx 30$, while the much smaller reflected fraction reaches three significant figures by $M \approx 18$ with a residual drift below 0.3% thereafter; the drift of S and A beyond $M = 30$ is confined to the fifth decimal place and is dominated by the slowly decaying rim-singularity tail of the radiation closure, not by the modal truncation itself. The same experiment repeated slightly away from the coalescence, at $\eta = \widetilde{\eta} + 0.05\,i$ with the standard expansion, settles at the same rate (from $S = 0.21733$ at $M = 6$ to $S = 0.21812$ at $M = 30$, with R and A correspondingly stable), so the truncation behaviour of the enhanced scheme at the exceptional point is indistinguishable from that of the standard scheme at a nearby regular lining: the extra sensitivity expected near the defective point is absorbed entirely by the augmented basis. The node counts n_{prop} and n_{tail} leave R, S, and A unchanged to eight decimal places for every value tested between 50 and 800 (Table 3), so the entries of Table 2 are controlled by M and $q_{\max}$ alone.

Table 2. Reflected, radiated, and absorbed fractions at the exceptional lining $\eta = \widetilde{\eta}$, $K = 3$, $L = 2$ (enhanced expansion) versus the modal order M, with the per-M adaptive spectral cutoff of Section 4; κ_2 is the two-norm condition number of the enhanced system (29).

M	R	S	A	$\lvert 1 - R - S - A \rvert$	κ_2
6	0.001153	0.212276	0.786935	3.6×10^{-4}	25
10	0.001169	0.212786	0.786135	9.0×10^{-5}	47
14	0.001174	0.212942	0.785921	3.7×10^{-5}	68
18	0.001176	0.213009	0.785834	1.9×10^{-5}	89
22	0.001177	0.213045	0.785789	1.1×10^{-5}	110
26	0.001178	0.213069	0.785760	7.3×10^{-6}	131
30	0.001178	0.213084	0.785743	5.0×10^{-6}	152
36	0.001179	0.213099	0.785725	3.2×10^{-6}	184
42	0.001179	0.213110	0.785713	2.1×10^{-6}	216

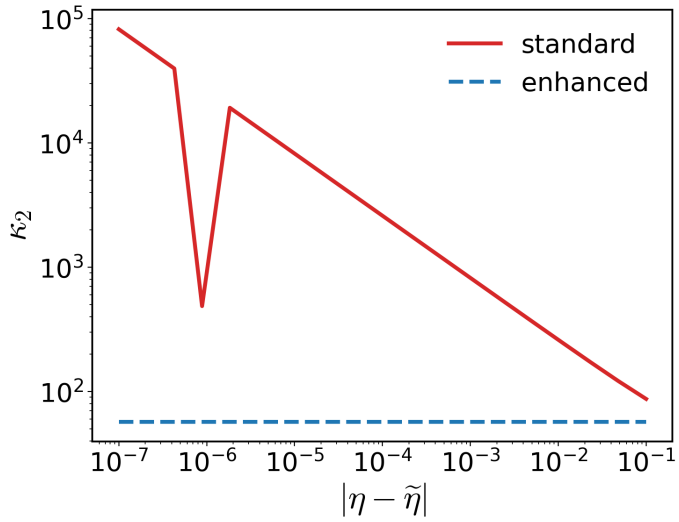


Figure 4. Two-norm condition number κ_2 of the matrix (29) as the lining approaches the exceptional point along $\eta = \widetilde{\eta} + i\,d$, $d \in [10^{-7}, 10^{-1}]$ on twenty logarithmically spaced points, with $K = 3$, $L = 2$, and $M = 12$. The solid curve is the standard scheme, whose condition number grows large and erratic near the coalescence as the defective basis becomes near-linearly dependent; the dashed horizontal line is the well-conditioned enhanced scheme at $\eta = \widetilde{\eta}$.

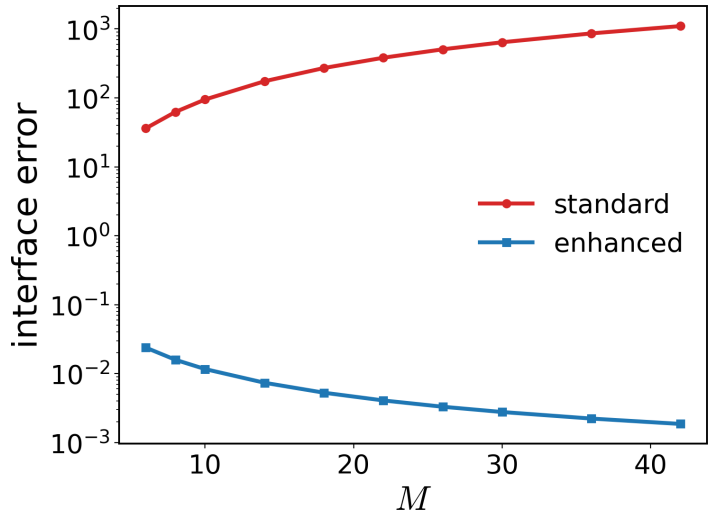


Figure 5. Pointwise interface error at $X = 0$ versus modal order $M \in \{6, 8, 10, 14, 18, 22, 26, 30, 36, 42\}$ at $\eta = \widetilde{\eta}$, $K = 3$, $L = 2$. Circles: standard; squares: enhanced.

The core of the validation is the pointwise reconstruction of every matching and boundary condition from the two sides of each interface. Figures 6 and 7 compare, on a uniform grid of 401 samples of $Y \in [-1, 1]$, the real part of the pressure and of the axial velocity in (10) at $X = 0$ as evaluated independently from the feed-side expansion (5) and from the lined-side expansion (19), at the exceptional lining $\eta = \widetilde{\eta}$, $K = 3$, $L = 2$, $M = 30$, with the enhanced scheme. Figure 8 performs the corresponding two-sided comparison of the first condition of (11) at the radiating mouth: the lined-side trace against the half-space trace $\mathcal{N}[v]$ of (12). This condition is imposed only through M projections, so its pointwise agreement measures convergence; the relative residual is 1.2×10^{-3} on $|Y| \leq 0.9$ (Table 1). Figure 9 completes the boundary audit with the rigid-flange condition of (2): the half-space normal velocity evaluated on the flange $1 < Y \leq 3$, normalised by the aperture-velocity rms, is at the level of 1.1×10^{-2} away from the mouth rim; the residual concentrates in a thin zone at the rim $Y \to 1^{+}$, and its structure is fully explained by the corner analysis: the fluid occupies a wedge of angle $3\pi/2$ at the rim, so the Meixner condition imposes the local behaviour $p - p_{\mathrm{rim}} = O(\rho^{2/3})$ in the distance ρ from the edge, hence an integrable velocity singularity $|\nabla p| = O(\rho^{-1/3})$ whose Fourier transform decays only like $|q|^{-2/3}$; a spectral representation truncated at $q_{\max}$ must therefore ring in an $O(1/q_{\max})$ neighbourhood of the rim, and the observed residual indeed decays away from the rim and with increasing cutoff. The exterior trace is even in Y to machine precision (1.2×10^{-16}). The convergence of all three pointwise residuals with the truncation is collected in Figure 10: the $X = 0$ and mouth residuals decrease monotonically, while the flange residual decreases more slowly, limited by the fixed spectral cutoff through the rim mechanism just described. In all cases, the two independent reconstructions are visually indistinguishable on the plotted scale, and the relative residuals are at the levels reported in Table 1. As a final consistency check of the exterior representation, the stationary-phase far field (32) agrees with direct quadrature of (9) on a semicircle at $Kr = 180$ to a worst relative deviation of 7.4×10^{-3}, and the directivity integral of (33) reproduces the flux value of S to 1.1×10^{-14}.

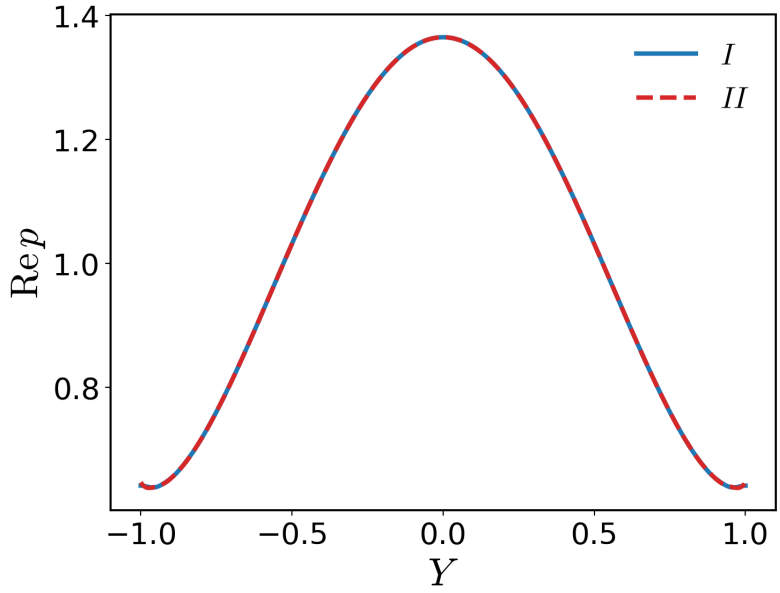


Figure 6. Pressure trace Re p at $X = 0$, reconstructed independently from the feed-side expansion (solid) and from the lined-side expansion (dashed), at the exceptional lining $\eta = \widetilde{\eta}$, $K = 3$, $L = 2$, with $M = 30$ retained modes in the enhanced scheme.

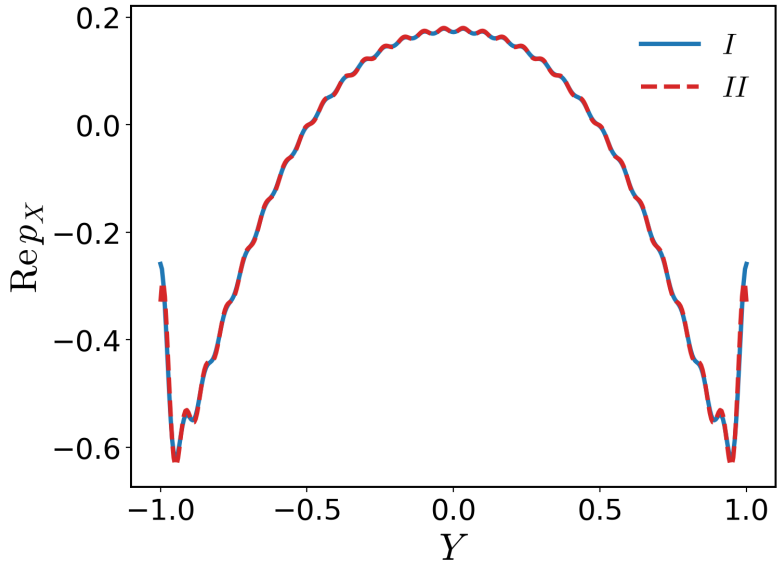


Figure 7. Axial-velocity trace Re $\partial_X p$ at $X = 0$, same configuration as Figure 6: feed side (solid) versus lined side (dashed).

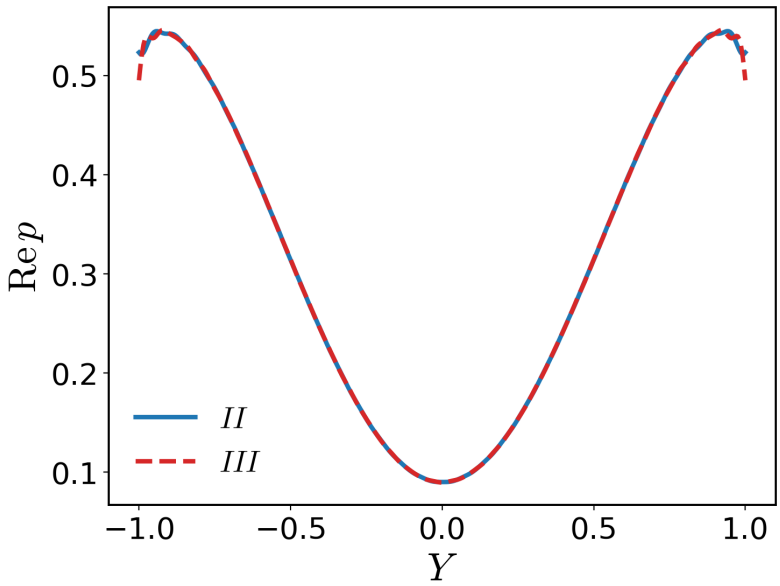


Figure 8. Pressure trace Re p at the radiating mouth $X = L$, reconstructed independently from the lined-side expansion (solid) and from the rigid-flange half-space trace $\mathcal{N}[v]$ of (12) (dashed), same configuration as Figure 6.

The conservation-law side of the validation is shown in Figure 11, in which the power-identity error $|1 - R - S - A|$ is plotted against the modal order M at the same reference (K, L, η) as in Figure 5. The enhanced scheme converges monotonically, reaching 5.0×10^{-6} at $M = 30$. The improper-integral side of the validation is shown in Figures 12 and 13: in Figure 12, the radiated power S is reported at $\eta = \widetilde{\eta}$, $K = 3$, $L = 2$, $M = 30$ as the cutoff $q_{\max}$ is varied from 0.7 to 2.2 times its adaptive value, and is stable to four significant figures at $S = 0.2131$ (the value at the reference adaptive cutoff, $q_{\max} \approx 45K$, is $S = 0.213084$, the entry of Table 1; raising the cutoff to 2.2 times its adaptive value lowers S by only 3×10^{-5}); the residual drift at the fifth figure decays algebraically with the cutoff, the signature of the slowly decaying spectral tail generated by the integrable corner singularity at the mouth rim. The radiated power is likewise insensitive, to ten significant figures, to the node counts n_{prop} and n_{tail} once these exceed one hundred. The spectral content underlying the

closure is shown in Figure 13, where the amplitude $|\tilde{v}(q)/\gamma(q)|$ of (12) is plotted against q at the same reference: the propagating band $|q| < K$ carries the radiated power, and the evanescent range carries a sequence of peaks near the real parts of the retained transverse wavenumbers, up to $q \approx M\pi$—the quantitative demonstration that the cutoff must clear the modal content, as built into the adaptive rule of Section 4.

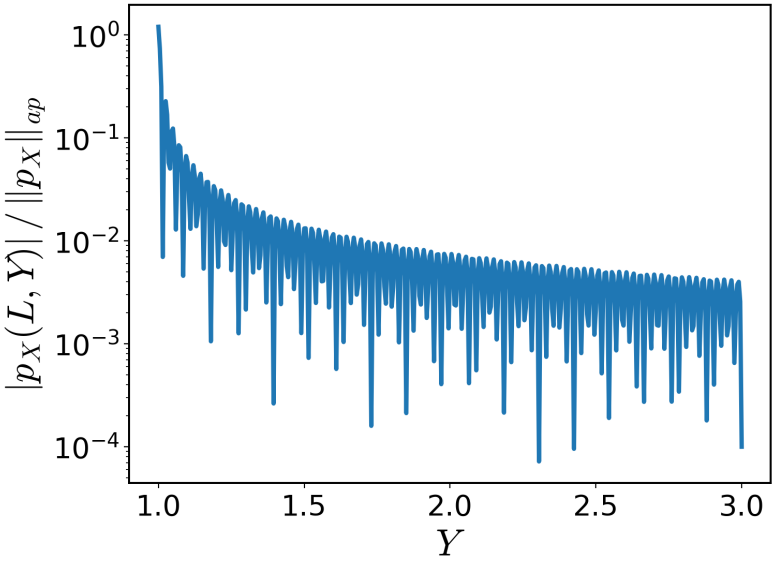


Figure 9. Rigid-flange condition: Magnitude of the half-space normal velocity on the flange $1 \le Y \le 3$ at $X = L$, normalised by the aperture-velocity rms, same configuration as Figure 6. The residual is confined to the integrable corner-singularity zone at the mouth rim and is at the 10^{-2} level beyond $Y = 1.1$.

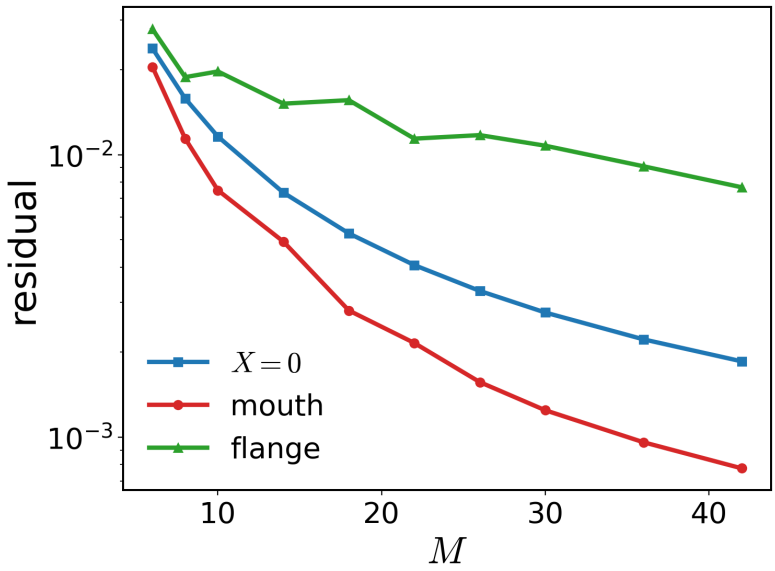


Figure 10. Convergence of the pointwise residuals of the enhanced scheme with the modal order $M \in \{6, 8, 10, 14, 18, 22, 26, 30, 36, 42\}$ at $\eta = \tilde{\eta}$, $K = 3$, $L = 2$: interface residual at $X = 0$ (squares), mouth pressure-continuity residual (circles), and flange-velocity residual (triangles).

Because the evanescent part of the spectrum carries no time-averaged power, the insensitivity of S understates the demands placed on the reactive part of the closure, and a direct quantitative assessment of the numerical integration error of the branch-aware rules is in order. Table 3 reports two experiments at the reference configuration. In the first, the cutoff is held at its adaptive value and the node counts are varied: relative to a reference

rule with $n_{\mathrm{prop}} = n_{\mathrm{tail}} = 1600$, the radiation-closure entries $N_{\ell k}^{\mathrm{rad}}$, their purely evanescent parts, and the evanescent (reactive) contribution to the reconstructed mouth-pressure trace all agree to better than 3×10^{-13} for every node count between 25 and 800: after the substitutions (22) and (23) every integrand is analytic, Gauss–Legendre converges geometrically, and the node-count error reaches the rounding floor already for a few tens of nodes per piece. The truncation of the far tail is therefore the only genuine integration error of the closure. In the second experiment, the node counts are held at 400 and the cutoff is varied: relative to a reference with 2.2 times the adaptive cutoff, the worst-case relative error of the radiation entries is 3.1×10^{-2} at 0.7 times the adaptive cutoff and 1.7×10^{-3} at the adaptive cutoff itself, while the reactive part of the mouth trace is reproduced to 2.0×10^{-3} at the adaptive cutoff, both errors decaying algebraically as the cutoff grows, consistent with the $|q|^{-2/3}$ rim-singularity tail of the aperture transforms. The evanescent contribution thus dominates the error budget of the closure precisely because it is invisible to the power balance; the adaptive cutoff rule keeps its effect on the reactive field at the 10^{-3} level while the radiated power stays stable to four significant figures (Figure 12).

Table 3. Quantitative integration-error assessment of the branch-aware spectral rules at the reference configuration ($\eta = \widetilde{\eta}$, $K = 3$, $L = 2$, $M = 30$). Top block: Worst-case relative error of the radiation entries $N_{\ell k}^{\mathrm{rad}}$, of their evanescent parts, and relative L^2 error of the reactive (evanescent) mouth-pressure trace, versus the node counts $n_{\mathrm{prop}} = n_{\mathrm{tail}} = n$ at the adaptive cutoff, relative to a 1600-node reference. Bottom block: The same error measures versus the cutoff factor $q_{\max}/q_{\max}^{\mathrm{ad}}$ at 400 nodes, relative to a reference with 2.2 times the adaptive cutoff, together with the radiated power.

	n	Entries N^{rad}	Evanescent Part	Reactive Trace
Node Counts	25–800	$<2 \times 10^{-13}$	$<3 \times 10^{-13}$	$<5 \times 10^{-14}$
	$q_{\max}/q_{\max}^{\mathrm{ad}}$	Entries N^{rad}	Reactive Trace	S
Cutoff	0.7	3.1×10^{-2}	3.9×10^{-3}	0.213141
	1.0	1.7×10^{-3}	2.0×10^{-3}	0.213082
	1.3	6.2×10^{-4}	1.2×10^{-3}	0.213065
	1.7	2.0×10^{-4}	6.6×10^{-4}	0.213056

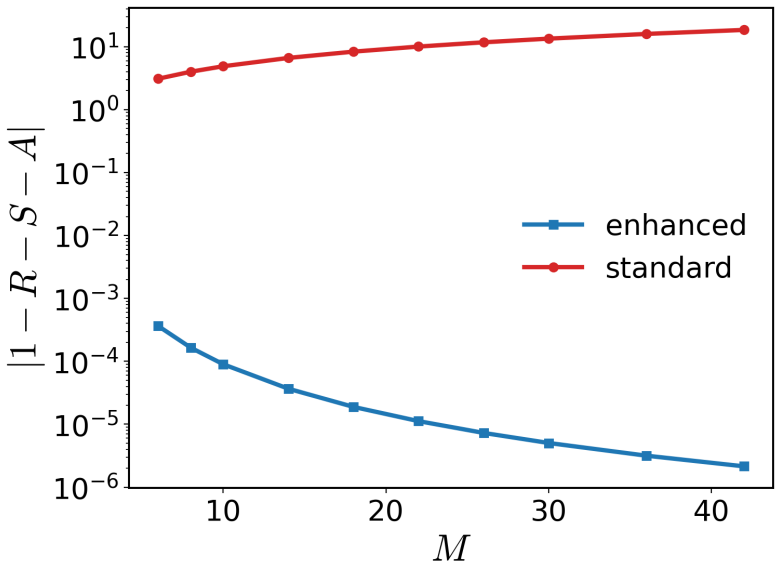


Figure 11. Power-identity error $|1 - R - S - A|$ versus modal order M at $\eta = \widetilde{\eta}$, $K = 3$, $L = 2$. Squares: enhanced; circles: standard.

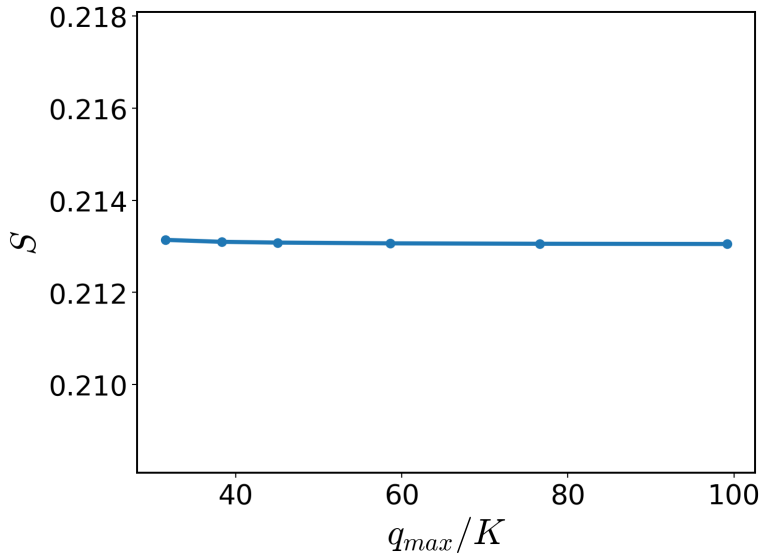


Figure 12. Radiated power S versus the spectral cutoff factor $q_{\max}/K$, varied from 0.7 to 2.2 times its adaptive value, at $\eta = \widetilde{\eta}$, $K = 3$, $L = 2$, $M = 30$ and $n_{\text{prop}} = n_{\text{tail}} = 400$. The value is stable to four significant figures, $S = 0.2131$, with an algebraically decaying residual drift from the rim-singularity tail.

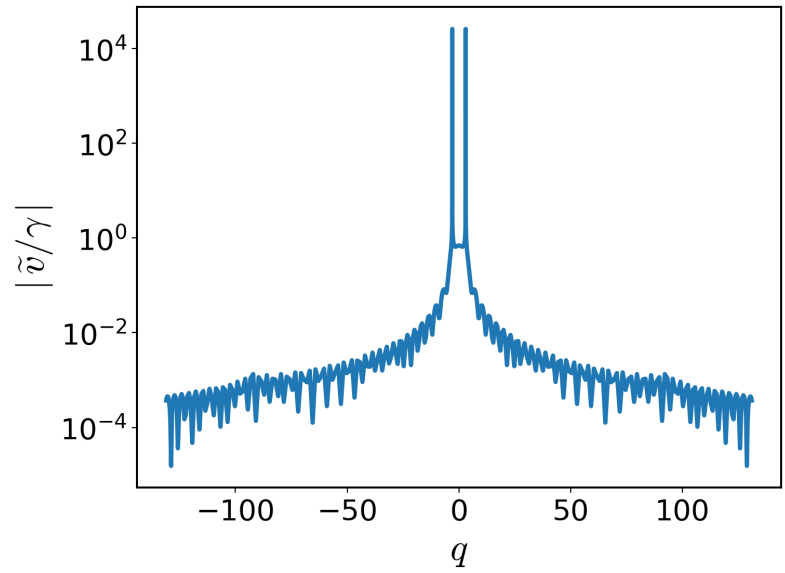


Figure 13. Spectral amplitude $|\tilde{v}(q)/\gamma(q)|$ of the rigid-flange closure (12) versus q at $\eta = \widetilde{\eta}$, $K = 3$, $L = 2$, $M = 30$. The propagating band $|q| < K$ carries the radiated power; the evanescent range shows peaks near the real parts of the retained transverse wavenumbers up to $q \approx M\pi$, which the adaptive cutoff of Section 4 must clear.

Figures 14–16 display the partition of power and the transmission loss along the frequency axis at the exceptional lining. Figure 14 plots R, S, A, and their sum versus the reduced frequency $K \in [1.4, 5.0]$ on a densely sampled grid at $\eta = \widetilde{\eta}$, $L = 2$, $M = 12$ with the enhanced scheme; the sum stays at unity to truncation accuracy, the reflected fraction is small over the whole band, the radiated fraction grows with K, and the absorbed fraction decreases correspondingly. The only non-smooth feature is a square-root cusp at $K = \pi$, marked by the dotted vertical line, where the first higher-order feed-duct mode ($\gamma_1 = \pi$) becomes cut-on and begins to carry reflected power; the partition is otherwise a smooth function of frequency. Figure 16 re-plots the transmission loss $\mathrm{TL} = -10 \log_{10} S$ from the same run, which decreases monotonically with frequency and inherits the same

cut-on cusp at $K = \pi$. Figure 15 performs the complementary sweep at fixed reference frequency, varying $\mathrm{Im}\,\eta$ across the window $[\mathrm{Im}\,\widetilde{\eta} - 0.18, \mathrm{Im}\,\widetilde{\eta} + 0.18]$ on thirty-one points at $\mathrm{Re}\,\eta = \mathrm{Re}\,\widetilde{\eta}$, $K = 3$, $L = 2$, $M = 12$, with the enhanced expansion used at the exceptional point and the standard simple-root expansion elsewhere; the absorbed and radiated fractions exchange smoothly through the coalescence, the energetic signature of the square-root branch structure of the two merging modes.

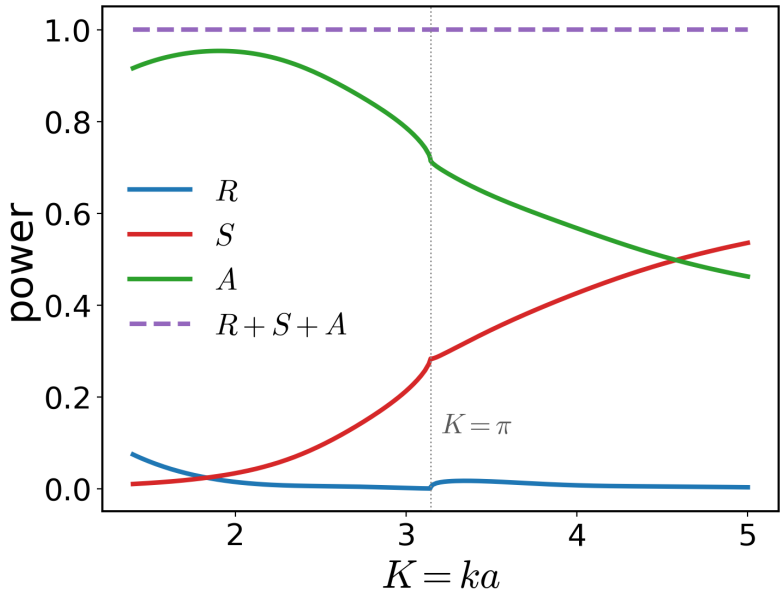


Figure 14. Reflected R, scattered S, absorbed A, and their sum versus the reduced frequency $K \in [1.4, 5.0]$, at $\eta = \widetilde{\eta}$, $L = 2$, $M = 12$, enhanced expansion. The dotted vertical line marks the $K = \pi$ cut-on of the first higher-order feed-duct mode, where R, S, and A show a square-root cusp; $R + S + A = 1$ throughout.

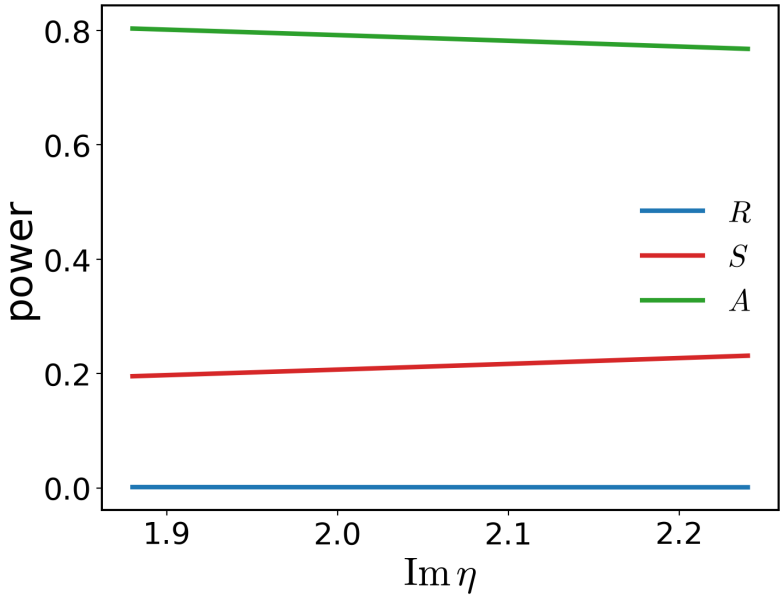


Figure 15. Reflected, scattered, and absorbed fractions versus $\mathrm{Im}\,\eta \in [\mathrm{Im}\,\widetilde{\eta} - 0.18, \mathrm{Im}\,\widetilde{\eta} + 0.18]$ on thirty-one points at $\mathrm{Re}\,\eta = \mathrm{Re}\,\widetilde{\eta}$, $K = 3$, $L = 2$, $M = 12$. The enhanced expansion is used at the exceptional point and the standard simple-root expansion away from it.

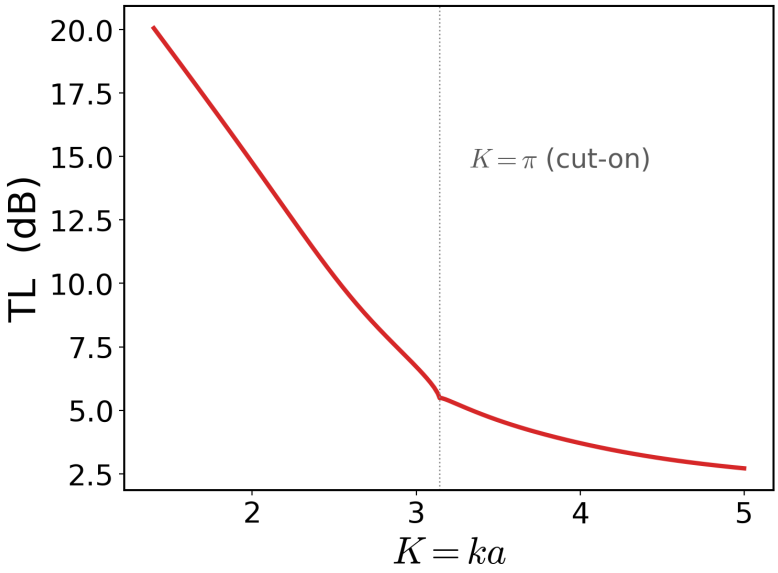


Figure 16. Transmission loss $\mathrm{TL} = -10 \log_{10} S$ versus reduced frequency K, same run as Figure 14. The dotted vertical line marks the $K = \pi$ feed-mode cut-on, the only non-smooth point of the curve.

The two-dimensional view of the power partition is given by the heatmaps of Figures 17 and 18. Both heatmaps fix $\mathrm{Re}\,\eta = \mathrm{Re}\,\widetilde{\eta}$ and $L = 2$ and scan a twenty-one-by-twenty-one grid of $(K, \mathrm{Im}\,\eta)$ with $K \in [1.6, 4.8]$ and $\mathrm{Im}\,\eta \in [\mathrm{Im}\,\widetilde{\eta} - 0.2, \mathrm{Im}\,\widetilde{\eta} + 0.2]$, at modal order $M = 12$. Near the exceptional admittance, the partition is governed almost entirely by frequency: the absorbed fraction is high at low K and decreases monotonically as K grows and radiation through the flange takes over, with only a weak dependence on $\mathrm{Im}\,\eta$ across this window. The reflected-power map stays small ($R \lesssim 0.05$) throughout and develops a shallow minimum along the $K = \pi$ cut-on line (dotted), consistent with the frequency sweep of Figure 14.

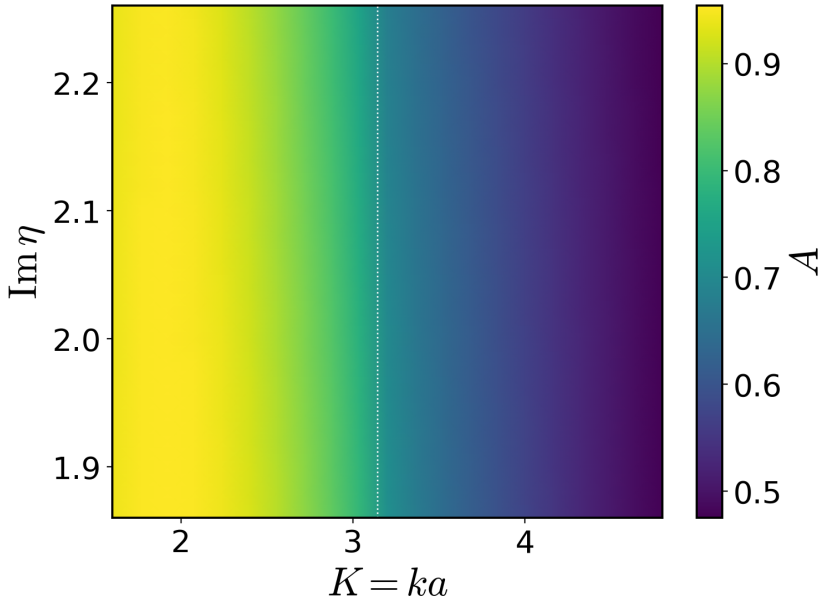


Figure 17. Absorbed power A on the $(K, \mathrm{Im}\,\eta)$-plane at $\mathrm{Re}\,\eta = \mathrm{Re}\,\widetilde{\eta}$, $L = 2$, $M = 12$, on a 21×21 grid with $K \in [1.6, 4.8]$ and $\mathrm{Im}\,\eta \in [\mathrm{Im}\,\widetilde{\eta} - 0.2, \mathrm{Im}\,\widetilde{\eta} + 0.2]$. The dotted line marks the $K = \pi$ feed-mode cut-on.

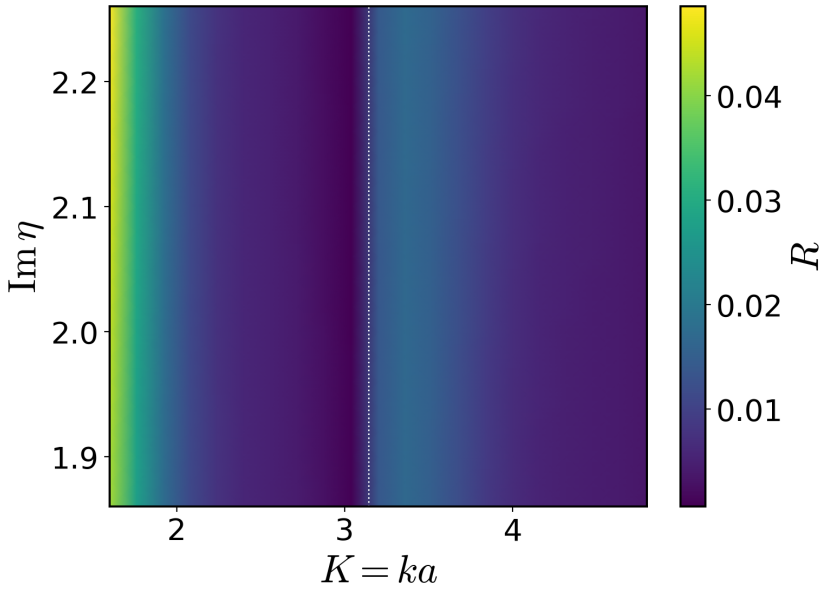


Figure 18. Reflected power R on the same parameter rectangle and grid as Figure 17, on a suppressed colour scale ($R \lesssim 0.05$). The dotted line marks the $K = \pi$ cut-on, along which R has a shallow minimum.

6.2. Independent Finite-Volume Verification

The validation reported so far, though it rests on the matching and boundary conditions themselves, is internal to the spectral formulation, and the rigid-limit cross-check exercises the radiation closure only at $\eta = 0$. As an external check of the full lined problem, the boundary-value problem (1)–(3) has been solved independently by a finite-volume frequency-domain method that shares no ingredient with the mode-matching solver: a formally second-order cell-centred finite-volume discretisation on the true two-region geometry, with homogeneous Neumann faces on the rigid walls, the flange, and the symmetry plane; the Robin condition (3) imposed through one-sided face extrapolation on the lined walls; a one-mode absorbing inlet boundary at $X = -8$ that injects the incident plane wave exactly and absorbs the reflected fundamental (all higher feed modes are evanescent at $K = 3$ and decay by $e^{-7.5}$ over the retained feed length); and a quadratic-profile perfectly matched layer of thickness 2, starting six half-widths beyond the mouth and above $Y = 7$, closing the half-space. The reflected fraction is extracted by projecting the computed field onto the fundamental feed mode at $X = -6$, the absorbed fraction from the lined-wall pressure trace, and the radiated fraction from the acoustic flux through the mouth plane. Table 4 compares the finite-volume power fractions on three successively halved grids, $h \in \{1/20, 1/40, 1/80\}$ (up to 5.2×10^5 unknowns), with the mode-matching values, for the rigid throat, the mildly absorbing lining $\eta = 0.6 + 0.6\,i$, and the exceptional lining $\eta = \widetilde{\eta}$, together with the observed convergence order of each entry, $p = \log_2\!\left[(u_h - u_{h/2})/(u_{h/2} - u_{h/4})\right]$, and its order-agnostic Aitken Δ^2 extrapolation. The fractions converge monotonically toward the mode-matching values under grid refinement in every case, though not uniformly at the formal second order of the scheme: in the two regular cases, the reflected fraction, controlled primarily by the smooth duct interior, converges with $p \approx 2.0$–2.1, whereas the radiated and absorbed fractions converge with $p \approx 1.7$—the order reduction expected from the $O(\rho^{2/3})$ Meixner behaviour at the mouth rim, which the integral functionals only partially average out. At the exceptional lining, all three fractions exhibit reduced orders of approximately 1.4, consistent with the square-root response of the degenerate transverse spectrum to perturbations, which amplifies the discretisation error of the lined-wall condition. Because the observed order

differs between entries, the tabulated extrapolations use the Aitken rule, which infers the rate from the data, rather than a fixed second-order Richardson formula; the extrapolated values agree with the spectral ones to within 8×10^{-5} in absolute terms on every fraction (3×10^{-4} or better in relative terms on every non-negligible fraction, and 0.7% or better on the small reflected fractions). The agreement covers the defective case itself: at $\eta = \widetilde{\eta}$ the finite-volume solution, which involves no modal basis and is therefore immune to the completeness failure of the standard expansion, confirms the enhanced-scheme fractions to the same accuracy as in the two regular cases.

Table 4. Independent finite-volume verification at $K = 3$, $L = 2$: Reflected, radiated, and absorbed fractions from the mode-matching (MM) solution ($M = 30$, enhanced at $\eta = \widetilde{\eta}$, standard otherwise) and from the finite-volume solver on three grids, together with the observed convergence order p estimated from the three grids and the order-agnostic Aitken Δ^2 extrapolation (extrap.). The rigid case has $A = 0$ identically.

Lining		MM	$h = 1/20$	$h = 1/40$	$h = 1/80$	p	Extrap.
$\eta = 0$	R	0.001654	0.002039	0.001752	0.001681	2.02	0.001658
	S	0.998346	0.998218	0.998305	0.998332	1.69	0.998344
$\eta = 0.6 + 0.6i$	R	0.003697	0.003973	0.003764	0.003716	2.12	0.003702
	S	0.539863	0.537220	0.539047	0.539618	1.68	0.539878
	A	0.456443	0.458898	0.457204	0.456668	1.66	0.456420
$\eta = \widetilde{\eta}$	R	0.001178	0.001009	0.001121	0.001162	1.45	0.001186
	S	0.213084	0.211244	0.212421	0.212870	1.39	0.213147
	A	0.785743	0.787511	0.786388	0.785950	1.36	0.785670

6.3. Field Maps and Optimisation in the Admittance Plane

The total acoustic field is reconstructed from (5), (19), and (9) over the full geometry, with the half-space contribution evaluated from the rigid-flange representation (9) on the same branch-aware quadrature used for the radiation entries; by construction, the plotted exterior field satisfies the flange condition, joins the throat field continuously across the mouth, and is even in the transverse coordinate. A baseline case is shown in Figure 19, computed at a mildly absorbing lining $\eta = 0.6 + 0.6\,i$, $K = 3$, $L = 2$, and $M = 30$ with the standard simple-root expansion, on the rectangle $X \in [-1.5, L + 3]$ and $Y \in [-1.8, 1.8]$; the lined-throat field exhibits the expected modal interference pattern, and the radiated field displays a clear forward beam, with finite, non-zero pressure along the rigid flange. Figure 20 shows the same geometry recomputed at the exceptional lining $\eta = \widetilde{\eta}$, $K = 3$, $L = 2$, and $M = 30$ with the enhanced expansion. Figure 21 shows that the same exceptional-point structure persists at higher frequencies—the same lining $\eta = \widetilde{\eta}$ and $L = 2$, but $K = 5$, with $M = 30$ and the enhanced expansion—and the radiated pattern develops the additional side lobes that the larger number of propagating feed modes makes available.

The far-field content of the same solutions is summarised by the directivity (33), shown in Figure 22 for the rigid throat, the mildly absorbing lining, and the exceptional lining at the reference frequency. The rigid throat radiates essentially the whole incident power in a broad forward beam. The mild lining roughly halves the forward level without reshaping the pattern appreciably. The exceptional lining suppresses the radiated fraction by almost a factor of five—most of the incident power is absorbed in the throat—and visibly flattens the pattern: the forward lobe is strongly reduced while the grazing-angle shoulders are relatively enhanced, reflecting the larger transverse content of the aperture velocity when the coalescing pair, rather than the plane-wave component, dominates the mouth field.

The area under each curve equals the corresponding radiated fraction, providing a further graphical statement of (33).

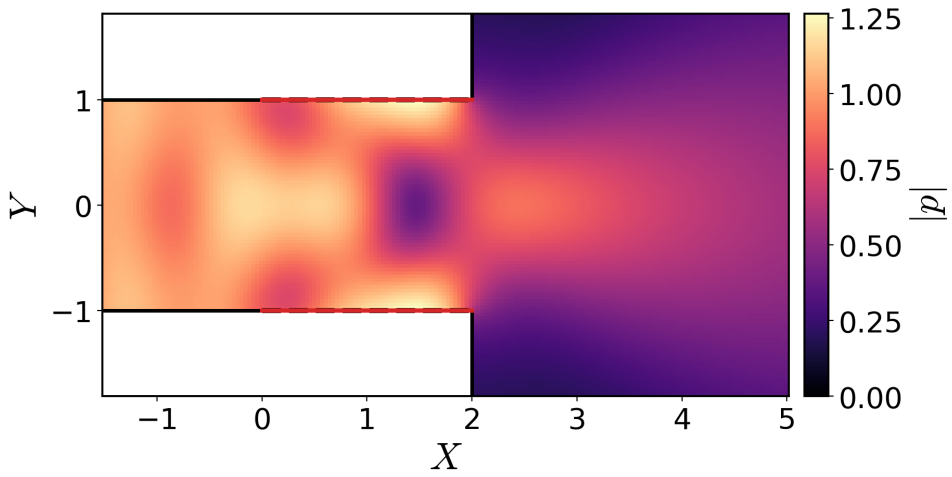


Figure 19. Pressure magnitude $|p(X, Y)|$ over the full geometry for the mildly absorbing lining $\eta = 0.6 + 0.6\,i$, at $K = 3$, $L = 2$, $M = 30$, standard expansion. The duct walls are drawn in black and the lined throat walls in red over a dashed underlay.

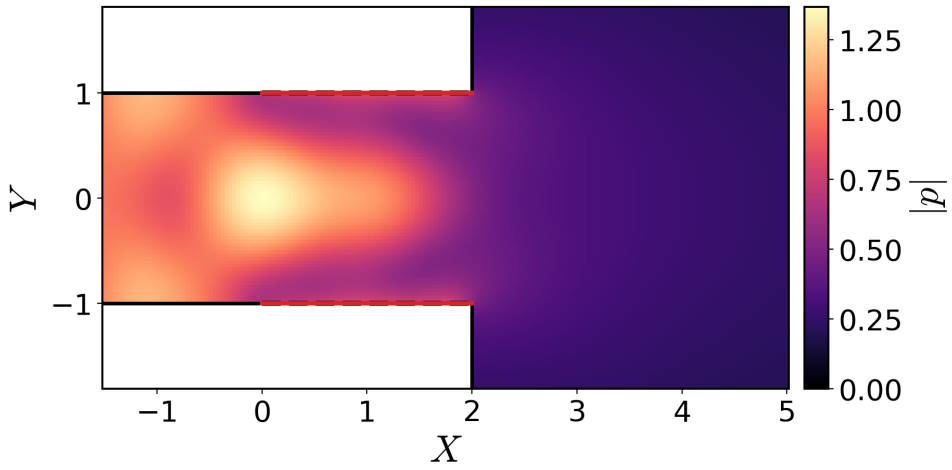


Figure 20. Pressure magnitude at the exceptional lining $\eta = \widetilde{\eta}$, $K = 3$, $L = 2$, $M = 30$, enhanced expansion.

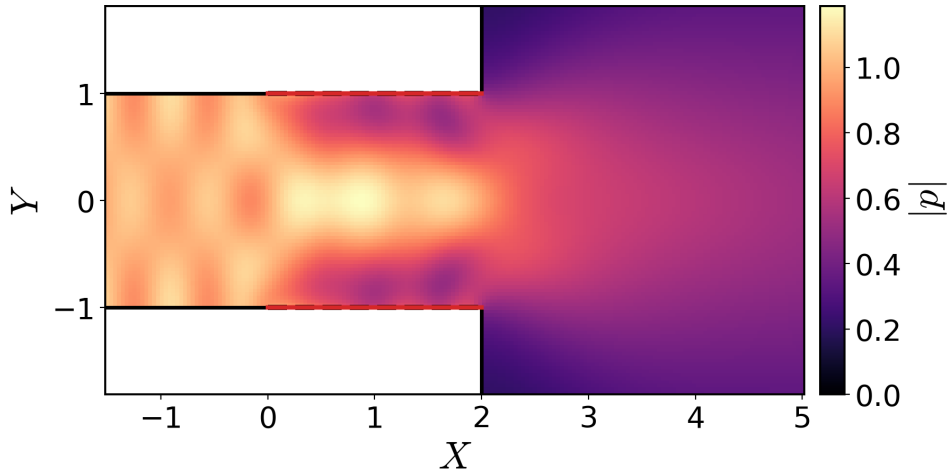


Figure 21. Pressure magnitude at the exceptional lining $\eta = \widetilde{\eta}$, $L = 2$, $M = 30$, enhanced expansion, at the higher reduced frequency $K = 5$.

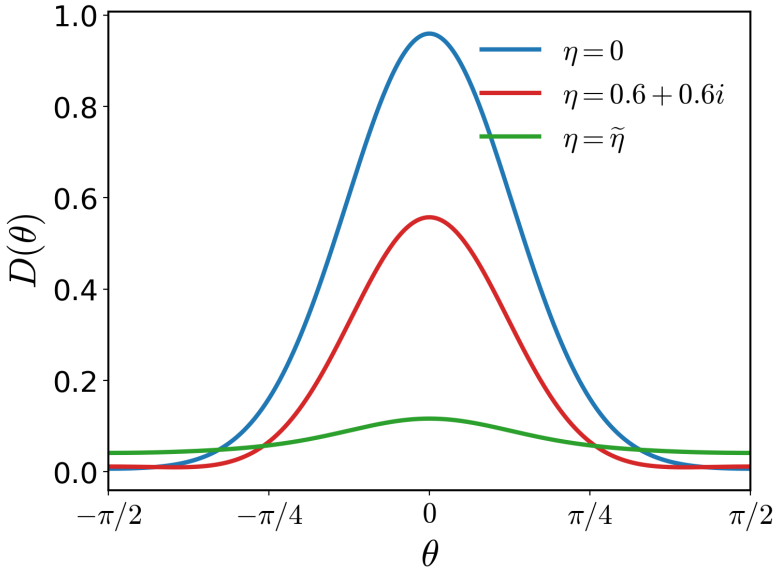


Figure 22. Far-field directivity $D(\theta)$ of (33) at $K = 3$, $L = 2$, $M = 30$ for the rigid throat ($\eta = 0$), the mildly absorbing lining $\eta = 0.6 + 0.6i$, and the exceptional lining $\eta = \widetilde{\eta}$ (enhanced expansion). The area under each curve is the radiated fraction S of that configuration.

The connection between the exceptional point and the optimum of the absorbed-power fraction is examined in Figures 23 and 24. The classical Cremer optimum [21–23,28] identifies the lining that maximises attenuation per unit length in a long uniform lined duct, and is itself a mode-merging condition; for a finite radiating throat such as the one studied here, the radiation through the flange perturbs that alignment and the optimum need not coincide exactly with the exceptional point. To quantify this, Figure 23 performs a two-dimensional scan of A over a window of the complex η-plane on a twenty-one-by-twenty-one grid that brackets both the exceptional point and the absorption optimum, with $\mathrm{Re}\,\eta \in [\mathrm{Re}\,\widetilde{\eta} - 0.70, \mathrm{Re}\,\widetilde{\eta} + 1.20]$ and $\mathrm{Im}\,\eta \in [\max(0.05, \mathrm{Im}\,\widetilde{\eta} - 1.75), \mathrm{Im}\,\widetilde{\eta} + 0.50]$, at $K = 3$, $L = 2$, and $M = 12$; the auto-selection rule uses the enhanced expansion at the exceptional point and the standard expansion away from it, and the few grid points at which the conserved-power identity fails by more than 10^{-2}, where the truncated model is no longer trustworthy, are discarded. The absorbed fraction forms a single interior ridge: it rises from the exceptional point toward larger $\mathrm{Re}\,\eta$ and smaller $\mathrm{Im}\,\eta$, attains an interior maximum, and falls away beyond it. The grid scan is then refined by an accurate local optimisation: a Nelder–Mead iteration started at the grid argmax converges, at $M = 12$, to $\eta_{\mathrm{opt}} = 2.2798 + 1.0668\,i$ with $A_{\mathrm{opt}} = 0.9019$, and repeating the refinement at $M = 20$ and $M = 30$ with the 400-node spectral quadrature moves the optimum by less than 1.1×10^{-3} in the admittance plane and 3.2×10^{-4} in the absorbed fraction, to the converged values $\eta_{\mathrm{opt}} = 2.2808 + 1.0669\,i$ and $A_{\mathrm{opt}} = 0.9016$; the location is insensitive to the quadrature node count (no movement at five digits between 180 and 400 nodes per piece). The refined optimum lies a distance $|\eta_{\mathrm{opt}} - \widetilde{\eta}| = 1.176$ from the exceptional point. This optimum exceeds the absorbed fraction at the exceptional point itself, $A(\widetilde{\eta}) = 0.7857$, by 11.58 percentage points: the radiation through the flange displaces the absorption optimum of the finite throat away from the Cremer-type mode-merging point. The path through the exceptional point at fixed $\mathrm{Re}\,\eta = \mathrm{Re}\,\widetilde{\eta}$, sampled on a sixty-three-point line over $\mathrm{Im}\,\eta \in [\mathrm{Im}\,\widetilde{\eta} - 0.30, \mathrm{Im}\,\widetilde{\eta} + 0.30]$ with $M = 12$, is shown in Figure 24: the absorbed, reflected, and scattered fractions exchange smoothly across the coalescence, the energetic signature of the underlying square-root branch structure, and the absorbed fraction remains high throughout the window about $\widetilde{\eta}$.

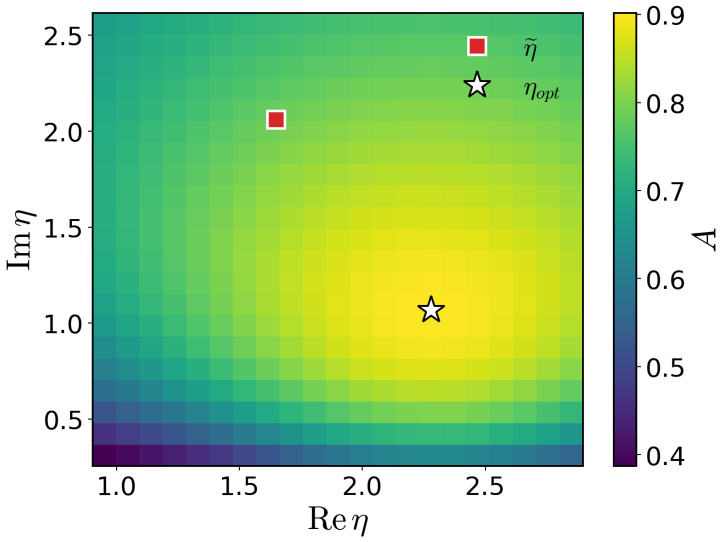


Figure 23. Absorbed-power fraction A over a twenty-one-by-twenty-one window of the complex admittance plane that brackets the exceptional point and the absorption optimum, at $K = 3$, $L = 2$, $M = 12$; grid points failing the conserved-power identity are masked. The red square marks the exceptional point $\widetilde{\eta}$; the white star marks the interior absorption optimum η_{opt} as refined by the Nelder–Mead local optimisation.

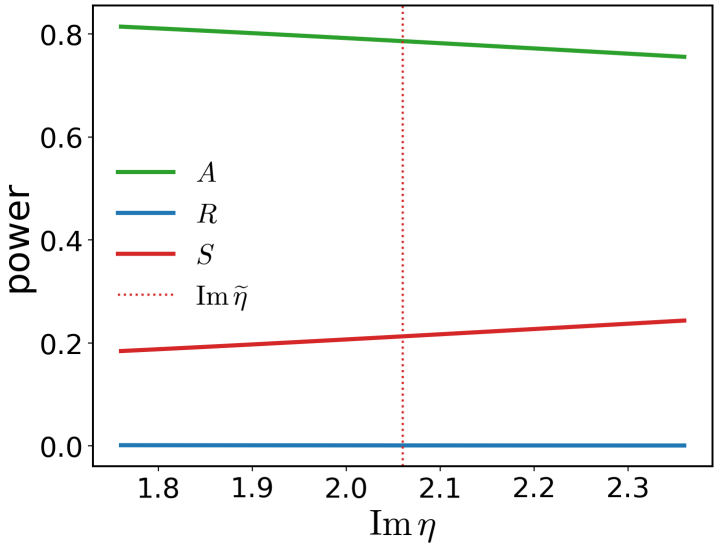


Figure 24. Reflected, scattered, and absorbed fractions along the path $\mathrm{Re}\,\eta = \mathrm{Re}\,\widetilde{\eta}$ on a sixty-three-point line in $\mathrm{Im}\,\eta \in [\mathrm{Im}\,\widetilde{\eta} - 0.30, \mathrm{Im}\,\widetilde{\eta} + 0.30]$ across the exceptional point (dotted vertical line) at $K = 3$, $L = 2$, $M = 12$.

6.4. Dependence on Throat Length and Frequency: The Origin of the Detuning

The results above are reported for the single reference geometry $(K, L) = (3, 2)$, and it is natural to ask whether the behaviour found near the exceptional point—the well-conditioned convergence of the augmented scheme and the detuning of the absorption optimum—is general or specific to that choice. Figure 25 repeats the computation at the exceptional lining across throat lengths $L \in [0.5, 8]$ at $K = 3$ with the enhanced expansion. The reflected fraction stays below 0.4% throughout; the radiated and absorbed fractions exchange monotonically, crossing near $L \approx 1.2$, and for long throats the absorbed fraction saturates ($A = 0.9984$ at $L = 6$) while the radiated fraction decays exponentially with the modal attenuation accumulated along the lined section ($S = 8.5 \times 10^{-4}$ at $L = 6$). The numerical behaviour of the augmented scheme is insensitive to the length: across the

whole range, the condition number of the enhanced system varies only between 63 and 54, and the maximal interface residual stays at 9×10^{-3} ($M = 12$), so nothing in the reported conditioning or convergence is specific to $L = 2$.

Figure 26 then repeats the admittance scan and the Nelder–Mead refinement of Section 6.3 for each length and tracks two measures of the detuning: the distance $|\eta_{\mathrm{opt}} - \widetilde{\eta}|$ and the absorption advantage $A_{\mathrm{opt}} - A(\widetilde{\eta})$. For $L \geq 1$, the distance decreases monotonically as the throat lengthens, from 1.78 at $L = 1$ through 1.18 at $L = 2$ and 0.58 at $L = 4$ to 0.30 at $L = 6$: as the radiated share of the power budget collapses, the optimum returns toward the mode-merging point, recovering the classical Cremer alignment of the long lined duct. The absorption advantage peaks near the crossover of the radiated and absorbed fractions (11.6 percentage points at $L = 2$) and collapses with the radiated share (1.5 points at $L = 4$, 0.08 points at $L = 6$); by $L = 8$ the absorption landscape is flat to 1.4×10^{-4} over a region containing $\widetilde{\eta}$, so the location of its argmax degenerates (open marker in Figure 26) while the advantage itself is negligible. In the opposite regime of short throats ($L \leq 1$), the lined section is too short to absorb efficiently ($A_{\mathrm{opt}} = 0.25$ at $L = 0.5$), and the optimum is governed almost entirely by the radiation loading of the mouth. The same mechanism operates along the frequency axis at fixed $L = 2$: at $K = 2$, where the radiated share at the exceptional lining is only $S = 0.033$, the refined optimum lies 0.74 from the exceptional point with an advantage of 2.2 points; at $K = 3$ ($S = 0.213$) the distance is 1.18 with 11.6 points; and at $K = 4$ ($S = 0.426$) the distance grows further to 1.64, the advantage (9.9 points) again being largest where absorption and radiation compete on comparable terms. The detuning of the absorption optimum from the exceptional point is therefore governed by the radiation loading of the finite mouth: the distance $|\eta_{\mathrm{opt}} - \widetilde{\eta}|$ grows with the radiated share of the power budget and vanishes, together with that share, as the throat lengthens toward the Cremer regime, while the throat length and the frequency enter through the radiated share they set (and, for the frequency, through the modal coupling at the mouth); the exceptional point itself, a property of the transverse spectrum alone, does not move. Alternative terminations—an unflanged pipe or a finite flange—would change the radiation load quantitatively through a different half-space kernel, shifting η_{opt} but not $\widetilde{\eta}$; their treatment requires the corresponding radiation closure (for example, the Levine–Schwinger unflanged kernel [20]) in place of (9) and is left as an extension; fluid–structure coupled scattering at the flanged junctions of flexible shells is examined in [40].

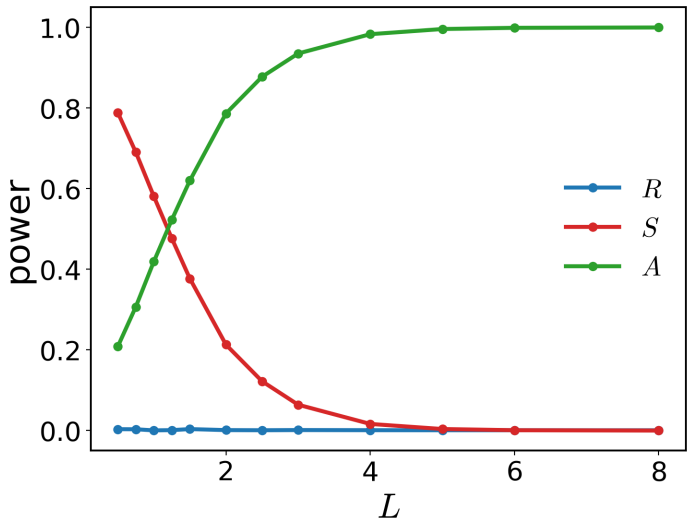


Figure 25. Reflected, radiated, and absorbed fractions at the exceptional lining $\eta = \widetilde{\eta}$ versus the throat length $L \in [0.5, 8]$ at $K = 3$, $M = 12$, enhanced expansion.

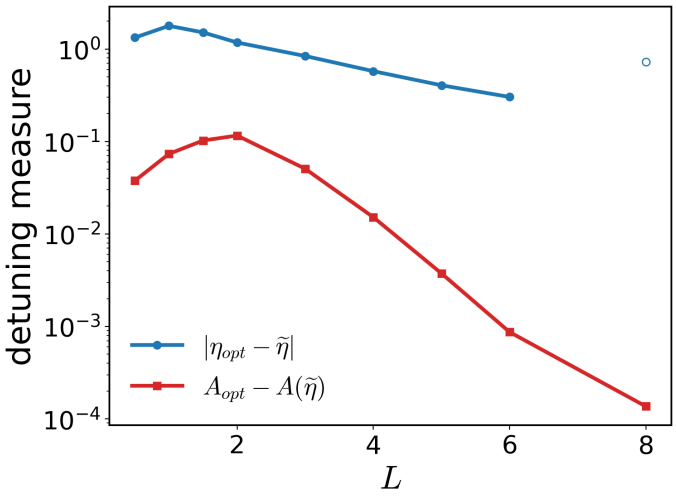


Figure 26. Detuning of the absorption optimum from the exceptional point versus the throat length at $K = 3$, $M = 12$: distance $|\eta_{\mathrm{opt}} - \widetilde{\eta}|$ (circles) and absorption advantage $A_{\mathrm{opt}} - A(\widetilde{\eta})$ (squares), both from the Nelder–Mead refinement of the admittance scan at each L. The open marker at $L = 8$ indicates the degenerate argmax of a landscape that is flat to 1.4×10^{-4} over a region containing $\widetilde{\eta}$.

6.5. Numerical Implementation Details

This closing subsection specifies every algorithmic parameter of the computations reported in this section, so that all numbers can be reproduced independently.

Root finding. The even roots of (13) are found by complex Newton iteration on F_e with relative step tolerance 10^{-14} and at most 80 iterations per seed. The seed list consists of $0.6 - 0.3\,i$, the perturbed rigid values $\ell\pi + 0.05 - 0.05\,i$ for $\ell = 1, \ldots, M + 9$, and, near the coalescence, the exceptional point $\widetilde{Q}$ itself, $\widetilde{Q} \pm 0.1$, and the two square-root split seeds of (21). Converged iterates are canonicalised to $\mathrm{Re}\, Q \geq 0$, accepted only if $|F_e(Q, \eta)| \leq 10^{-7}(1 + |Q|)$, and de-duplicated at absolute tolerance 10^{-6} (it is this de-duplication that retains a single copy of the double root at exactly $\eta = \widetilde{\eta}$; see the discussion of Figure 4). The exceptional point is constructed, never hardcoded: Newton iteration on the analytic function $H(Q) = \partial_Q F_e$ from the seed $2.1 - 1.1\,i$, followed by $\widetilde{\eta} = -\widetilde{Q} \tan \widetilde{Q}$, with the residuals $|F_e|$, $|\partial_Q F_e|$, $|N|$, and $|\partial_Q^2 F_e - 2|$ verified at machine zero on every run.

Argument-principle certification. The canonical root count is certified with (20) applied to the entire function $G = \cos Q\, F_e$ on the rectangle $[10^{-3}, M\pi + 1.137] \times [-6\,i, 6\,i]$ (corners displaced off the axes), each side discretised by the trapezoidal rule with 1400 points; the integer count is required to be at least the number of retained roots.

Spectral quadrature. The composite rule of Section 4 uses $n_{\mathrm{prop}} = 400$ Gauss–Legendre nodes on $\theta \in [-\pi/2, \pi/2]$, $n_{\mathrm{tail}} = 400$ nodes per side on $t \in [0, \operatorname{arcosh} 3]$, and a far-tail Gauss–Legendre rule on $[3K, q_{\max}]$ with 3 nodes per unit of q plus 32, where $q_{\max} = \max\bigl(8K,\ 1.35 \max_n |\mathrm{Re}\, Q_n| + 8\bigr)$ adapts to the retained modal content; parameter sweeps use 180-node rules. All transverse integrals over $[-1, 1]$ use 360-point Gauss–Legendre quadrature (400-point quadrature for the power and trace diagnostics).

Linear algebra and residuals. The $3M \times 3M$ system (29) is solved by LU factorisation with partial pivoting; condition numbers are two-norm values computed by singular value decomposition. Pointwise residuals are relative L^2 norms on 401 uniform samples: at $X = 0$ over the full aperture, at the mouth on $|Y| \leq 0.9$, on the flange as the rms of the normal velocity over $1.1 \leq Y \leq 3$ normalised by the aperture-velocity rms, and for the symmetry residual, as the odd-in-Y content of the exterior mouth trace.

Independent implementations. The rigid-limit cross-check uses a separate implementation of the classical flanged-guide problem (its own derivation, quadrature, and

linear system) with 48 modes, 800-node propagating and tail rules, and cutoff $4K$. The finite-volume verification of Section 6.2 uses the formally second-order cell-centred scheme described there, on grids up to $h = 1/80$ (5.2×10^5 unknowns), with inlet boundary at $X = -8$, measurement plane at $X = -6$, free half-space of extent 6 beyond the mouth and 7 above the axis, and perfectly matched layers of thickness 2 with stretch $s = 1 + 5\,i\,(d/2)^2$, solved by sparse LU factorisation; the reported extrapolations use the order-agnostic Aitken Δ^2 rule on the three grids, with the observed convergence order estimated from the same data.

7. Conclusions

A non-self-adjoint boundary-value problem for acoustic radiation from an impedance-lined flanged duct has been analysed at an order-two exceptional point of the transverse spectrum, by extending the augmented mode-matching ansatz of Lawrie et al. [8] from junctions closed by discrete modal sets to an open mouth closed by the radiation continuum of a flanged half-space. The exceptional point has been constructed from the simultaneous vanishing of the characteristic function and of its first derivative with respect to the transverse spectral parameter, its order-two property certified in closed form, and the defectiveness of the ordinary expansion quantified by a non-conjugated norm integral that vanishes there. The half-space closure has been generated by the spectrum of the aperture velocity, so that the rigid-flange condition and the velocity continuity across the mouth hold exactly by construction, and pressure continuity is imposed by projection; the resulting improper integrals have been evaluated by branch-aware substitutions, with a spectral cutoff tied to the largest retained transverse wavenumber. Validation has been carried out on the matching and boundary conditions themselves—pointwise two-sided reconstruction of pressure and velocity at the internal junction, of pressure at the radiating mouth, of the vanishing normal velocity on the flange, and of the transverse symmetry of the exterior field—together with the analytic reduction of the rigid limit to the classical flanged-duct radiation problem, cross-checked against an independent implementation of that problem, and the full lined problem—including the defective case—has been verified against an independent finite-volume solution of the same boundary-value problem, whose grid-converged fractions agree with the mode-matching values for rigid, mildly absorbing, and exceptional linings; a conserved-power identity has been derived and monitored as a necessary check, the evanescent spectrum carrying no time-averaged power so that a power balance alone cannot detect an error in the reactive part of a radiation closure. The numerical experiments set the degenerate standard expansion against the well-conditioned augmented one in the radiating setting. A scan of the absorbed-power fraction over the complex admittance plane, refined by local optimisation to $\eta_{\mathrm{opt}} = 2.2808 + 1.0669\,i$ with $A_{\mathrm{opt}} = 0.9016$, locates an interior absorption optimum at a lining clearly detuned from the exceptional point, exceeding the absorbed fraction at the exceptional point by more than ten percentage points: for a finite radiating throat, the radiation loading displaces the optimum away from the Cremer-type mode-merging condition. A parametric study across throat lengths and frequencies shows that this detuning is governed by the radiation loading of the finite mouth: it grows with the radiated share of the power budget and vanishes as the throat lengthens toward the long-duct Cremer regime, the exceptional point itself—a property of the transverse spectrum alone—remaining fixed. Natural extensions include asymmetric linings and surface-wave families [41], multisectioned and axisymmetric geometries [12,42], trifurcated elastic-shell chambers [43], bifurcated circular waveguides with reacting liners [44], structural variations and sound-source modelling in the presence of absorbent materials [29], fully coupled vibroacoustic walls, in which the locally reacting lining is replaced by an elastic membrane, plate, or lattice-cored shell, and

the transverse spectrum couples to structural wave propagation [15,30,35], and admittance models constrained by experimental data.

Funding: The project was funded by the KAU Endowment (WAQF) at King Abdulaziz University, Jeddah, Saudi Arabia. The author, therefore, gratefully acknowledges WAQF and the Deanship of Scientific Research (DSR) for their technical and financial support.

Data Availability Statement: The original contributions presented in this study are included in the article. Further inquiries can be directed to the corresponding author.

Acknowledgments: The project was funded by the KAU Endowment (WAQF) at King Abdulaziz University, Jeddah, Saudi Arabia. The author, therefore, gratefully acknowledges WAQF and the Deanship of Scientific Research (DSR) for their technical and financial support.

Conflicts of Interest: The author declares no conflicts of interest.

References

1. Bender, C.M.; Boettcher, S. Real spectra in non-Hermitian Hamiltonians having $\mathcal{PT}$ symmetry. *Phys. Rev. Lett.* **1998**, *80*, 5243–5246. [CrossRef]
2. Trefethen, L.N.; Embree, M. *Spectra and Pseudospectra: The Behavior of Nonnormal Matrices and Operators*; Princeton University Press: Princeton, NJ, USA, 2005.
3. Heiss, W.D. The physics of exceptional points. *J. Phys. A Math. Theor.* **2012**, *45*, 444016. [CrossRef]
4. Berry, M.V. Physics of nonhermitian degeneracies. *Czech. J. Phys.* **2004**, *54*, 1039–1047. [CrossRef]
5. Miri, M.-A.; Alù, A. Exceptional points in optics and photonics. *Science* **2019**, *363*, eaar7709. [CrossRef]
6. Özdemir, Ş.K.; Rotter, S.; Nori, F.; Yang, L. Parity–time symmetry and exceptional points in photonics. *Nat. Mater.* **2019**, *18*, 783–798. [CrossRef]
7. Achilleos, V.; Theocharis, G.; Richoux, O.; Pagneux, V. Non-Hermitian acoustic metamaterials: Role of exceptional points in sound absorption. *Phys. Rev. B* **2017**, *95*, 144303. [CrossRef]
8. Lawrie, J.B.; Nennig, B.; Perrey-Debain, E. Analytic mode-matching for accurate handling of exceptional points in a lined acoustic waveguide. *Proc. R. Soc. A* **2022**, *478*, 20220484. [CrossRef]
9. Morse, P.M.; Ingard, K.U. *Theoretical Acoustics*; McGraw-Hill: New York, NY, USA, 1968.
10. Pierce, A.D. *Acoustics: An Introduction to Its Physical Principles and Applications*, 3rd ed.; Springer: Cham, Switzerland, 2019.
11. Rienstra, S.W.; Hirschberg, A. *An Introduction to Acoustics*; Lecture Notes IWDE 92-06; Eindhoven University of Technology: Eindhoven, The Netherlands, 2021.
12. Munjal, M.L. *Acoustics of Ducts and Mufflers*, 2nd ed.; Wiley: Chichester, UK, 2014.
13. Nawaz, R.; Yaseen, A.; Alahmadi, H.; Tiryakioglu, B. A mode-matching analysis of flexible shells and waveguides with partitioning and muffler conditions. *Int. J. Mech. Mater. Des.* **2024**, *20*, 1009–1028. [CrossRef]
14. Mittra, R.; Lee, S.W. *Analytical Techniques in the Theory of Guided Waves*; Macmillan: New York, NY, USA, 1971.
15. Lawrie, J.B.; Afzal, M. Acoustic scattering in a waveguide with a height discontinuity bridged by a membrane: A tailored Galerkin approach. *J. Eng. Math.* **2017**, *105*, 99–115. [CrossRef]
16. Afzal, M.; Akhtar, N.; Alkinidri, M.O.; Shutaywi, M. A mode-matching tailored-Galerkin approach for higher order interface conditions and geometric variations. *Mathematics* **2023**, *11*, 755. [CrossRef]
17. Bilal, H.; Afzal, M. On the extension of the mode-matching procedure for modeling a wave-bearing cavity. *Math. Mech. Solids* **2022**, *27*, 348–367. [CrossRef]
18. Afzal, M.; Satti, J.U.; Wahab, A.; Nawaz, R. Scattering analysis of a partitioned membrane-bounded cavity with material contrast. *J. Acoust. Soc. Am.* **2022**, *151*, 31–44. [CrossRef]
19. Eom, H.J. *Wave Scattering Theory: A Series Approach Based on the Fourier Transformation*; Springer: Berlin/Heidelberg, Germany, 2001.
20. Levine, H.; Schwinger, J. On the radiation of sound from an unflanged circular pipe. *Phys. Rev.* **1948**, *73*, 383–406. [CrossRef]
21. Cremer, L. Theorie der Luftschalldämpfung im Rechteckkanal mit schluckender Wand und das sich dabei ergebende höchste Dämpfungsmaß. *Acustica* **1953**, *3*, 249–263.
22. Tester, B.J. The optimization of modal sound attenuation in ducts, in the absence of mean flow. *J. Sound Vib.* **1973**, *27*, 477–513. [CrossRef]
23. Tester, B.J. The propagation and attenuation of sound in lined ducts containing uniform or 'plug' flow. *J. Sound Vib.* **1973**, *28*, 151–203. [CrossRef]
24. Kato, T. *Perturbation Theory for Linear Operators*; Classics in Mathematics; Springer: Berlin/Heidelberg, Germany, 1995.

25. Midya, B.; Konotop, V.V. Modes and exceptional points in waveguides with impedance boundary conditions. *Opt. Lett.* **2016**, *41*, 4621–4624. [CrossRef]
26. Taha, H.H.; Yaseen, A.; Elsadig, M. TM scattering by an impedance-loaded rectangular groove: An enhanced computational mode-matching formulation. *Opt. Laser Technol.* **2026**, *204*, 116129. [CrossRef]
27. Afzal, M.; Shafique, S. Attenuation analysis of flexural modes with absorbent lined flanges and different edge conditions. *J. Acoust. Soc. Am.* **2020**, *148*, 85–99. [CrossRef]
28. Afzal, M.; Ahmed, N.; Safdar, M.; Kurkcu, H. Optimizing acoustic liner conditions for noise control: A study of flexible components and restraint conditions. *Chaos Solitons Fractals* **2024**, *185*, 115091. [CrossRef]
29. Afzal, M.; Ahmed, N.; Safdar, M.; Umar, M. On the modeling of sound sources in waveguides with structural variations and sound-absorbent materials. *Commun. Nonlinear Sci. Numer. Simul.* **2025**, *145*, 108714. [CrossRef]
30. Afzal, M.; Yaseen, A.; Safdar, M. Fluid–structure interaction in coaxial lined chambers with membrane discs: Mode-matching tailored Galerkin approach. *Int. J. Mech. Mater. Des.* **2025**, *21*, 1017–1035. [CrossRef]
31. Afzal, M.; Safdar, M.; Alahmadi, H.N. Analyzing the impact of flexible shells and sound absorbent lining on acoustic wave behavior in ducts. *Math. Methods Appl. Sci.* **2024**, *47*, 10462–10477. [CrossRef]
32. Lawrie, J.B.; Afzal, M. Higher mode filtering: Optimum attenuation in a continuum of exceptional points. *Proc. R. Soc. A* **2026**, *482*, 20250811. [CrossRef]
33. Nawaz, R.; Yaseen, A.; Alkinidri, M.O. Fluid–structure coupled response of dynamical surfaces tailored in a flexible shell. *Math. Mech. Solids* **2023**, *28*, 2404–2419. [CrossRef]
34. Alruwaili, A.D.; Afzal, M.; Alahmadi, H.N.; Wahab, A. Wave scattering in cylindrical waveguides: Analyzing flexible shells and liner conditions. *Alex. Eng. J.* **2024**, *91*, 610–619. [CrossRef]
35. Zarastvand, M.R.; Abdoli, E.; Talebitooti, R. A lattice metamaterial-based sandwich cylindrical system for numerical simulation approach of vibroacoustic transmission considering triply periodic minimal surface. *Appl. Math. Mech. (Engl. Ed.)* **2025**, *46*, 2035–2054. [CrossRef]
36. Davis, P.J.; Rabinowitz, P. *Methods of Numerical Integration*, 2nd ed.; Academic Press: Orlando, FL, USA, 1984.
37. Boyd, J.P. *Chebyshev and Fourier Spectral Methods*, 2nd ed.; Dover: Mineola, NY, USA, 2001.
38. Alahmadi, H.; Afzal, M.; Javeed, U.; Nawaz, T. Analytical study of mode filtering in a duct with resistive layers. *PLoS ONE* **2026**, *21*, e0339192. [CrossRef]
39. Trefethen, L.N. *Approximation Theory and Approximation Practice*, Extended ed.; SIAM: Philadelphia, PA, USA, 2019. [CrossRef]
40. Alkuhayli, N.; Yaseen, A.; Alrashdi, A. Fluid-structure coupled wave scattering in a flexible cylindrical shell with flanged junctions. *J. Vib. Eng. Technol.* **2026**, *14*, 29. [CrossRef]
41. Rienstra, S.W. A classification of duct modes based on surface waves. *Wave Motion* **2003**, *37*, 119–135. [CrossRef]
42. Zorumski, W.E. *Acoustic Theory of Axisymmetric Multisectioned Ducts*; NASA TR R-419; National Aeronautics and Space Administration: Washington, DC, USA, 1974.
43. Afzal, M.; Safdar, M. Mode-matching technique for analyzing scattering in elastic shell chambers: Applications in trifurcated waveguide systems. *Commun. Nonlinear Sci. Numer. Simul.* **2024**, *130*, 107723. [CrossRef]
44. Alkuhayli, N.; Yaseen, A.; Nawaz, R.; Alahmadi, H. Acoustic scattering and mode interaction in bifurcated circular waveguide structures with reacting liners and discontinuities. *PLoS ONE* **2025**, *20*, e0321050. [CrossRef]

Disclaimer/Publisher's Note: The statements, opinions and data contained in all publications are solely those of the individual author(s) and contributor(s) and not of MDPI and/or the editor(s). MDPI and/or the editor(s) disclaim responsibility for any injury to people or property resulting from any ideas, methods, instructions or products referred to in the content.